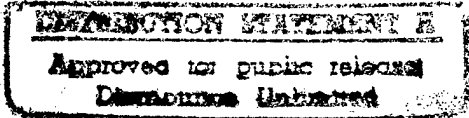


REPORT DOCUMENTATION PAGE			Form Approved OMB No. 0704-0188	
Public reporting burden for this collection of information is estimated to average 1 hour per response, including the time for reviewing instructions, searching existing data sources, gathering and maintaining the data needed, and completing and reviewing the collection of information. Send comments regarding this burden estimate or any other aspect of this collection of information, including suggestions for reducing this burden, to Washington Headquarters Services, Directorate for Information Operations and Reports, 1215 Jefferson Davis Highway, Suite 1204, Arlington, VA 22202-4302, and to the Office of Management and Budget, Paperwork Reduction Project (0704-0188), Washington, DC 20503.				
1. AGENCY USE ONLY (Leave Blank)	2. REPORT DATE 4/8/97	3. REPORT TYPE AND DATES COVERED FINAL Technical 20 Dec 93 - 19 Dec 96		
4. TITLE AND SUBTITLE Optoelectronic Materials Center		5. FUNDING NUMBERS MDA972-94-1-0003		
6. AUTHORS S.R.J. Brueck, J. Harris, N. Peygambarian, et al				
7. PERFORMING ORGANIZATION NAME(S) AND ADDRESS(ES) The Regents of the University of New Mexico Center for High Technology Materials 1313 Goddard SE Albuquerque, NM 87106		8. PERFORMING ORGANIZATION REPORT NUMBER 3-4029X		
9. SPONSORING / MONITORING AGENCY NAME(S) AND ADDRESS(ES) DARPA/ETO 3701 North Fairfax Drive Arlington, VA 22203		10. SPONSORING / MONITORING AGENCY REPORT NUMBER MDA972-94-1-0003		
11. SUPPLEMENTARY NOTES				
12a. DISTRIBUTION / AVAILABILITY STATEMENT UNLIMITED		12b. DISTRIBUTION CODE		
<div style="text-align: center;">  </div>				
13. ABSTRACT (Maximum 200 words) <p>Work in the three focus areas of the OMC: Diode-based Visible Sources ((DVS), Optoelectronic Tools for Intelligent Manufacturing (OTIM), and Optoelectronic Information Networks (OIN) is detailed in the following final technical report. The efforts in DVS concentrated on the development of GaN materials and device technology and the realization of blue and near uv sources by Quasi Phase Matched (QPM) Second Harmonic Generation (SHG). Significant results were achieved in both areas including the demonstration of a blue (~ 425 nm) single quantum well GaN/InGaN diode and SHG waveguide devices with 20 mW of power in the blue. Under the OITM focus area, research concentrated on the development of tunable diode laser sources for use in spectroscopy. Success in the demonstration of widely tunable devices based on quantum well engineering was achieved. In the OIN focus area work was aimed at a variety of optoelectronic functions that are required for the successful demonstration of optical interconnects. Work addressed quantum well based optical modulators, high speed extended wavelength silicon MSM detectors, holographic interconnects and smart pixels based on resonant enhanced detectors, heterojunction bipolar transistors and VCSELs. Smart pixel arrays with switching speeds of 1 Gb/sec were demonstrated.</p>				
14. SUBJECT TERMS Optoelectronic tools, OTIM, OIN, Second Harmonic Generation		15. NUMBER OF PAGES 56		
		16. PRICE CODE NSP		
17. SECURITY CLASSIFICATION OF REPORT UNCLASSIFIED	18. SECURITY CLASSIFICATION OF THIS PAGE UNCLASSIFIED	19. SECURITY CLASSIFICATION OF ABSTRACT UNCLASSIFIED	20. LIMITATION OF ABSTRACT UL	

19970411 020

Sponsored by

DEFENCE ADVANCED RESEARCH PROJECTS AGENCY

OPTOELECTRONIC MATERIALS CENTER

FINAL REPORT

FOR THE PERIOD DECEMBER 20, 1993 TO DECEMBER 19, 1996

A Collaborative Program including

**Center for High Technology Materials
of the University of New Mexico**

Stanford University

University of Arizona

Sandia National Laboratories

MIT Lincoln Laboratory

DARPA Order No. A230/00

Issued by DARPA/CMO under contract #MDA972-94-1-0003

The views and conclusions contained in this document are those of the authors and should not be interpreted as representing the official policies, either express or implied of the Defense Advanced Research Projects Agency or the U.S. Government.

Focus Area: Diode-based Visible Sources**Task: Group III-Nitrides****(505-277-1358, shersee@chtm.eece.unm.edu)****(415-723-9775, harris@luciano.stanford.edu)****Personnel**

S. Hersee (PI)

J. S. Harris(PI)

L. F. Lester

K. Malloy

M. Osinski

N. Peyghambarian

Summary

The OMC has applied a "holistic" strategy to its III-N visible diode sources program. OMC team members at UNM, SU, ASU and SNL have in parallel addressed AlGaInN materials, III-N specific process technology and the reliability of III-N based visible-diodes, all of which are necessary for the successful fabrication of visible diode sources. In many instances this work has been in collaboration with industry partners, who have provided not only R&D resources but also a valuable perspective view that has enabled us to identify and address the important III-N issues.

This program includes work on MOCVD and MBE epitaxial growth of AlInGa_N, advanced microstructural XRD analysis, a study of III-N luminescence, process technology development (including RIE etching, contact metalization, laser facet preparation), LED device characterization and failure mode analysis performed on commercially available GaN based LEDs.

In March 1996 the OMC demonstrated a InGa_N quantum well LED emitting at 423 nm.

1. MOCVD Growth and XRD Characterization of AlInGa_N

UNM began III-N materials research in 1992 and use a dedicated, horizontal-geometry, RF-heated, warm wall MOCVD reactor for AlInGa_N growth. The reactor features a custom gas flow separator that eliminates group III and group V premixing before the reaction zone. It was found that important structural and electrical properties of thick III-N epilayers were critically controlled by the initial buffer layer growth, and it was realized that the buffer layer therefore has a direct impact on the reproducibility and manufacturability of III-N materials and devices. AFM and XRD measurements on buffer layers revealed that after deposition of the buffer at low temperature, there was a significant redistribution and recrystallization of the deposited material during the ramp to the higher (normal) growth temperature. The redistribution of the buffer material exhibited the behavior of a Stranski-Krastanov process and this hypothesis has allowed us to understand the columnar nature of the III-N epitaxial layers. It is now generally agreed that III-N layers grown on sapphire are in fact polycrystalline with grains on the order of 100's of angstroms. Within each polycrystal the semiconductor can be of high quality and exhibits little strain, however, the polycrystals have slightly different orientations and this causes the large rocking curve typically observed for III-N materials.

Alloy growth has also presented challenges but we have now mastered the growth of InGa_N with InN mole fractions up to 34%. Growth temperature was found to be the most convenient parameter for controlling the In incorporation and growth temperatures between 720 and 800 C resulted in In_{0.34}Ga_{0.66}N and In_{0.1}Ga_{0.9}N respectively. For high InN mole fractions growth rate also played a role, and it was found that slightly more In could be incorporated by keeping the TMIn flow constant and raising the TMGa. The temperature and growth rate dependence of indium incorporation indicate that indium evaporation from the growth surface is the rate limiting process for In incorporation during InGa_N growth.

XRD reciprocal space mapping of this InGa_N showed it to have approximately the same mosaicity (range of tilt in "c" axis) as the surrounding Ga_N. This is expected based on the columnar polycrystalline nature of the III-N film but to our knowledge this is the first time that the InGa_N mosaicity has been measured.

We have grown several designs of GRINSCH and SCH, single and multiple quantum well InAlGa_N heterostructures. PL and XRD measurements indicate that for some structures In can redistribute from the quantum wells during post growth annealing at 700 C (e.g. as used for magnesium activation.) We are continuing to explore this extremely important area, which has direct relevance to device efficiency and reliability.

2. VPE Growth for Ga_N Substrates

One of the major challenges facing widespread Nitride materials is lack of a lattice matched, electrically conducting substrate. Vapor phase epitaxy (VPE) of Ga_N has a long history and has been widely used for Ga_N growth because of its high growth rates of up to a few tens of $\mu\text{m/hr}$ and lack of carbon incorporation into the film. This approach is thus an alternative to very high pressure bulk growth to realize Ga_N substrates. In conventional chloride transport VPE of Ga_N, the Ga source is gallium monochloride (GaCl), which is stable only at temperatures above 600 C and is produced by the reaction of liquid gallium with hydrogen chloride (HCl) gas. The supply of GaCl is controlled by the Ga temperature and the flow rates of the HCl and H₂ carrier gas. In this work, we used gallium trichloride (GaCl₃) as the Ga source. Ammonia (NH₃) and nitrogen (N₂) gases were used as the nitrogen source and carrier gas, respectively. H₂ and HCl gases were not used. Many researchers have reported VPE growth of GaAs using GaCl₃, however the GaCl₃ was reduced to GaCl before crystal synthesis.

An open flow horizontal quartz tube with single zone hot wall furnace was used as the reactor. The actual GaCl₃ vapor supply was about 0.003 slm and 1.0 - 1.5 slm of NH₃ and 1.5 ~ 2.0 slm of N₂ were introduced into the reactor. The resulting V/III ratio was about 500 to 700. The growth temperature (T₁) was varied over the range of 930 ~ 1050 C. Atmospheric pressure was maintained during the growth.

Thermodynamic analysis of the various reactions revealed that under typical Ga_N growth conditions, the driving force for etching is much higher than that for deposition. A thick deposition of GaCl₃ is always observed on the exhaust side of the reactor which implies that

GaCl_3 vapor did not react with ammonia and thus the etching reaction may be negligible. Therefore, the growth of GaN was governed by the GaCl reaction rather than GaCl_3 reaction.

Growth of GaN using the above GaCl_3 precursor and reactions was investigated under a variety of growth conditions on (0001) sapphire substrates. After loading the substrates, the reactor was pumped and purged with high purity nitrogen. The substrates were heated to the growth temperature under a NH_3/N_2 ambient. According to XPS analysis, the sapphire surface was nitrified during this heating phase. After reaching the growth temperature, GaCl_3 was supplied to the reactor using nitrogen carrier gas. No low temperature buffer layer was used in these experiments.

X-ray diffraction was used to determine the crystallinity and the orientation of the GaN films. Only (0001) type plane peaks are observed in the 2 θ / ω X-ray diffraction pattern for thick GaN films on sapphire. This implies that the GaN film and sapphire substrate basal planes are parallel to each other, i.e. $\text{GaN} \langle 0001 \rangle // \text{sapphire} \langle 0001 \rangle$. The measured c-lattice parameter of the GaN film was 5.192 Å, which is slightly larger than the literature value, 5.1850 ± 0.0005 Å. This indicates that the GaN film is under compressive stress from the differential thermal expansion coefficients of GaN and sapphire. Only one set of reflection peaks from the (10 $\bar{1}$ 1) plane is observed with 60° spacing in a ϕ -scan. This indicates that the GaN films grown on sapphire are single crystal. The angular position of the GaN (10 $\bar{1}$ 1) peaks are well matched to the sapphire (11 $\bar{2}$ 3) peaks. This means the GaN crystal is rotated 90° around the c-axis to minimize the lattice mismatch strain, i.e. $\text{GaN} \langle 10\bar{1}0 \rangle // \text{sapphire} \langle 11\bar{2}0 \rangle$.

In order to characterize the optical properties of GaN films, photoluminescence (PL) measurements were done at both room temperature and 77 K. At room temperature, only band edge emission near 3.40 eV was observed. At 77 K, the spectrum consisted of several peaks including an exciton bound to a neutral donor (I_2), an exciton bound to a neutral acceptor (I_1) and donor-acceptor pairs. The spectrum dominated by I_2 emission near 3.47 eV. The band edge emission peak had a FWHM of 60 meV at room temperature and the exciton bound to donor emission peak had a FWHM of 25 meV at 77 K. A very weak deep level luminescence band near 2.1 eV was also observed at both room temperature and 77 K. According to the PL spectra, the thick GaN films grown by VPE using GaCl_3/N_2 and NH_3/N_2 have good crystalline quality.

Scanning Electron Microscopy (SEM) was used to characterize the surface morphologies of GaN films grown on c-sapphire substrates. Commonly, it is very difficult to achieve a very smooth surface over a large area in chloride VPE growth of GaN films due to its high deposition and gas phase etching rates. The localized flux uniformity and growth temperature play key roles in determining the surface morphologies of GaN films. In this experiment, we fixed V/III ratio at approximately 500. The position of the sapphire substrate (1 inch distant from the NH_3/N_2 nozzle) and the configuration of the GaCl_3/N_2 and NH_3/N_2 nozzles were also fixed to optimal positions. The effect of the growth temperature on surface morphology of GaN films was investigated. For GaN films grown below 950 C, the surface was covered by GaN crystallites (islands) with an approximate size of a few microns. These islands did not coalesce and there are holes all the way to the substrate. The 2 θ / ω scan of X-ray diffraction shows only (0001) type

plane peaks with broad FWHM. The PL spectra shows only band edge emission at room temperature which implies that each GaN crystallite has good crystal quality. According to the X-ray f-scan, several different in-plane orientations were observed. This means each crystallite has different in-plane orientation.

As the growth temperature was increased to 975 C, crystallites coalesced to one another and the surface became smoother, however, grooves and microholes which have about $50 \sim 60^\circ$ inclined sidewalls were observed. The films grown at this temperature regime have narrower X-ray diffraction and photoluminescence linewidths. The surface morphologies of films grown at similar temperatures (965 C) with a 3 times longer growth time confirms that the film has grown laterally, rather than three dimensionally. From the f-scan of the GaN (10 $\bar{1}$ 2) peak, the film is single crystal. The smoothest and flattest surface morphology of a GaN film is achieved by growth at 995 C. At the boundary of two laterally grown islands, thin shallow grooves are observed. Higher growth temperature and longer growth time appear to give better surface morphologies. According to Hall measurements, GaN films have high n-type background conductivity up to $10^{19}/\text{cm}^3$. The electron mobility at room temperature is in the range of 40 to 90 cm^2/Vs .

ZnO has a lattice mismatch less than 2% to GaN, thus a ZnO buffer layer should produce better surface morphology and lower dislocation densities than GaN grown directly on sapphire substrates. The other advantage of ZnO buffer layer is the possibility of fabricating GaN "substrates" by first growing a thick GaN layer on ZnO and then etching away the ZnO layer since ZnO can easily be etched by any acid and bulk GaN is not etched by acids. In order to achieve high quality GaN, it is important to optimize the growth and study the properties of the ZnO buffer layer.

Single crystalline ZnO layers are grown on c-cut sapphire substrates by pulsed laser deposition (PLD). The optimum growth conditions are at a temperature of 550 C and oxygen partial pressure of 0.01 T. In-situ RHEED pattern of the ZnO film is taken along [11 $\bar{2}$ 0] direction, as shown in Figure 1. Sharp and Streaky RHEED pattern indicates atomically smooth surface and good crystallinity of ZnO film. From the PL measurement at 77K, near-band-edge emission is observed at 3.34 eV with a FWHM of 89 meV. In addition, there is no low energy peak which is usually associated with structural imperfection.

Substrate temperature and nitrogen partial pressure are found to be critical for the growth of GaN films on sapphire substrates by PLD. Below 400 C, the films are amorphous but the crystallinity is greatly improved with increasing substrate temperature. Single crystal GaN films are obtained above 700 C. The FWHM of GaN (0002) peak decreases with increasing temperature and 0.37° is obtained for a film grown at 800 C and 0.01 Torr nitrogen. From the transmission spectra, the optimum nitrogen pressure during growth appears to be at 0.01 Torr. For growth pressures as low as 10^{-4} Torr, the GaN films are of poor quality. For the films grown at 725 C under a nitrogen pressure of 0.01 Torr, greater than 80% transmission is obtained. At 0.45 Torr, the films are yellow with more particulates on the surface of the films.

At 750 C and 0.01 Torr nitrogen, a single crystal GaN film was grown on a sapphire substrate with a thin ZnO buffer layer. The transmission spectra estimates the band-gap energy of 3.37 eV and the thickness of 420 nm for the GaN film, which corresponds to the growth rate of 0.12 Å/pulse. A sharp and streaky RHEED pattern indicates an atomically smooth surface and good crystallinity.

We then employed ZnO films as a buffer layers for GaN growth by vapor phase epitaxy (VPE). Strong dependence on buffer layer thickness is observed in both surface morphology and X-ray measurements of GaN films. The VPE-grown GaN film directly on sapphire shows strong three dimensional island growth. The surfaces of GaN films grown on ZnO with the thickness of 25-50 nm exhibits a terrace like flat surface, suggesting enhanced two dimensional growth. In addition, buffer layer thickness up to 50 nm improves the crystalline quality with a strong band-edge peak in PL spectra. Cracks and peeling-off are observed for GaN films on 200nm-thick ZnO buffer layers. These films also exhibit a broader XRC peak width and broad band PL which originates from the diffusion of Zn into GaN. We, therefore, conclude that the optimized thickness of ZnO buffer layer is around 25-50 nm.

3. Chemical precursors for gas source MBE

One of the major challenges for growth of GaN is the high equilibrium partial pressure of nitrogen over GaN which requires that a high nitrogen chemical potential be present in order to achieve film growth. This makes it difficult to grow GaN at low pressure, and is particularly problematic for growing GaN by molecular beam epitaxy (MBE), a growth technique that requires an ultra-high vacuum. The two contradictory needs- a high nitrogen chemical potential and a low pressure- can only be resolved by using a highly active source of nitrogen. The most important issue in the MBE growth of nitrides is the need for a suitable source of active nitrogen.

During the course of the OMC program, we developed a reliable MBE growth technology for the III-V nitrides. Films are grown in a specially modified Varian GEN II MBE machine which is dedicated to nitrides. Most of our research has focused upon finding the best (i.e. most reactive) source of nitrogen for MBE. We have investigated physically excited nitrogen, in the form of an electron cyclotron resonance (ECR) plasma, as well as two chemical sources: hydrogen azide (HN_3) and dimethylhydrazine ($(\text{CH}_3)_2\text{N}_2\text{H}_2$). Standard effusion cells are used for Group III elements. Films are grown on c-plane sapphire. Before the growth, the substrate is nitridized for half an hour and a low-temperature GaN or AlN buffer layer is deposited. The substrate is then heated up to the final growth temperature. Such parameters as substrate temperature, V-III ratio, nitridation, and buffer layer are being varied in order to determine the optimum growth conditions.

Films are characterized by a variety of techniques, including optical transmission, X-ray diffraction, photoluminescence, Raman spectroscopy, spectroscopic ellipsometry, and X-ray photoelectron spectroscopy. We have found that, in general, films grown with chemical sources display much smoother and more uniform surfaces than those grown with an ECR plasma. Hydrogen azide gives the highest growth rates ($\sim 0.25 \mu\text{m/hr}$), and films grown with HN_3 have

consistently shown strong bandedge PL even at room temperature, with very little of the midgap (~2.2 eV) luminescence that dominates most GaN PL spectra.

However, azide-grown films demonstrate high background carrier concentrations and low mobilities, which we attribute to impurities in the source gas (which is not commercially available and must be manufactured in the lab). Films grown with dimethylhydrazine (DMH₂) have lower apparent impurity concentrations than those grown with HN₃, but also have lower growth rates which we attribute to incomplete thermal cracking of the source gas.

Our work with hydrogen azide (HN₃) clearly demonstrated the value in finding a chemical nitrogen sources for growth of high-quality GaN. However, the extreme danger of HN₃ makes finding a less explosive alternative a necessity.

4. Optical and Electrical Characterization of InGaAlN

We report on the electrical and optical characterization of GaN and GaInN. Hall measurements have been used to electrically characterize the n-type Si doped GaN, p-type Mg doped GaN and unintentionally doped GaN. Unintentionally doped samples show room temperature electron concentrations of 10^{17} cm^{-3} and mobility's of $580 \text{ cm}^2 \text{ V}^{-1} \text{ s}^{-1}$, peaking at $960 \text{ cm}^2 \text{ V}^{-1} \text{ s}^{-1}$ at 150 K. Si-doped samples typically show room temperature mobility's of $340 \text{ cm}^2 \text{ V}^{-1} \text{ s}^{-1}$ with electron concentrations above 10^{18} cm^{-3} , and activation energies of 10 meV for these doping levels. Mg-doped samples showed room temperature mobility's of $19 \text{ cm}^2/\text{Vs}$ with hole concentrations of 10^{17} cm^{-3} after annealing at 700 C for 30 minutes in an N₂ ambient. The hole concentration had an activation energy of 184 meV.

Optical characterization of the GaN and GaInN have been performed using a CW argon laser, a quadrupled Nd:YAG laser, and a doubled mode locked Ti:Sapphire laser which is tunable from 350 nm to 500 nm. A strong GaN bandedge emission is present under both pulsed and CW pumping conditions. Yellow emission is only observed in undoped GaN and Si doped GaN when the pumping source is the CW argon laser or the Ti:Sapphire laser. The YAG laser has revealed possible impurity transitions in annealed and unannealed Mg doped GaN with energies near the electrical activation energy.

Photoluminescence and photoluminescence excitation (PLE) experiments have been performed on GaN at both room temperature and low temperature using the tunable Ti:Sapphire laser. It has been observed that at room temperature the yellow intensity of GaN at a fixed photon flux peaks at a pump wavelength of 368 nm (below the gap) with an excitation half width of 2.5 nm. The yellow emission becomes very weak by a pump wavelength of about 450 nm. This peak has been associated with neutral donor absorption. Low temperature measurements show the emergence of a broad absorption peak which is associated with donor-acceptor pair absorption. The dependence of output yellow intensity on input power has been observed to rise from a square root dependence to a near linear dependence as the pump wavelength is varied from 350 nm to 450 nm.

Photoluminescence has also been used to characterize the GaInN. The bandgap energy at low temperature versus indium composition has been fitted suggesting a large bowing parameter. The

temperature dependence of both GaN and GaInN bandgap energy has been described using Bose-Einstein formula. Clear evidence has shown that the Varshni fitting formula, which is valid for most of the semiconductor materials, does not work for the temperature dependence of GaN and GaInN bandgap energy. The deep level transition peak associated and GaInN bandedge have been observed to move together with the GaInN bandgap at various temperatures. Annealing experiments (700 C, 20 min) have shown that indium composition does not change with annealing, but non-radiative recombination may be enhanced after annealing.

5. Non-destructive Evaluation Techniques for Nitrides

The nitrides present a different set of challenges compared to prior investigations of III-V materials. Two new techniques have been extensively developed: variable angle spectroellipsometry and micro Raman/PL. The variable angle spectroellipsometry was described in considerable detail in earlier reports. The new micro PL/RAMAN setup allows us to map PL and RAMAN spectra with a spatial resolution of 1 μm . The variations in peak position, peak width, peak intensity, and area under the peak are monitored in the out-of-plane and the in-plane directions of the film. This is done for various peaks simultaneously.

The combination of high spatial resolution RAMAN and PL is particularly useful to study the crystalline microstructure in GaN. RAMAN permits the measurement of strains in the film, crystallographic orientation, and free carrier concentration.

In the following graph, we compared the quality of an MBE and a VPE grown sample using the new micro RAMAN setup. The A_1 (LO) mode is damped by plasmons in the VPE grown sample, so this sample has a larger electron concentration. Also the peaks are sharper and better resolved for the MBE grown sample.

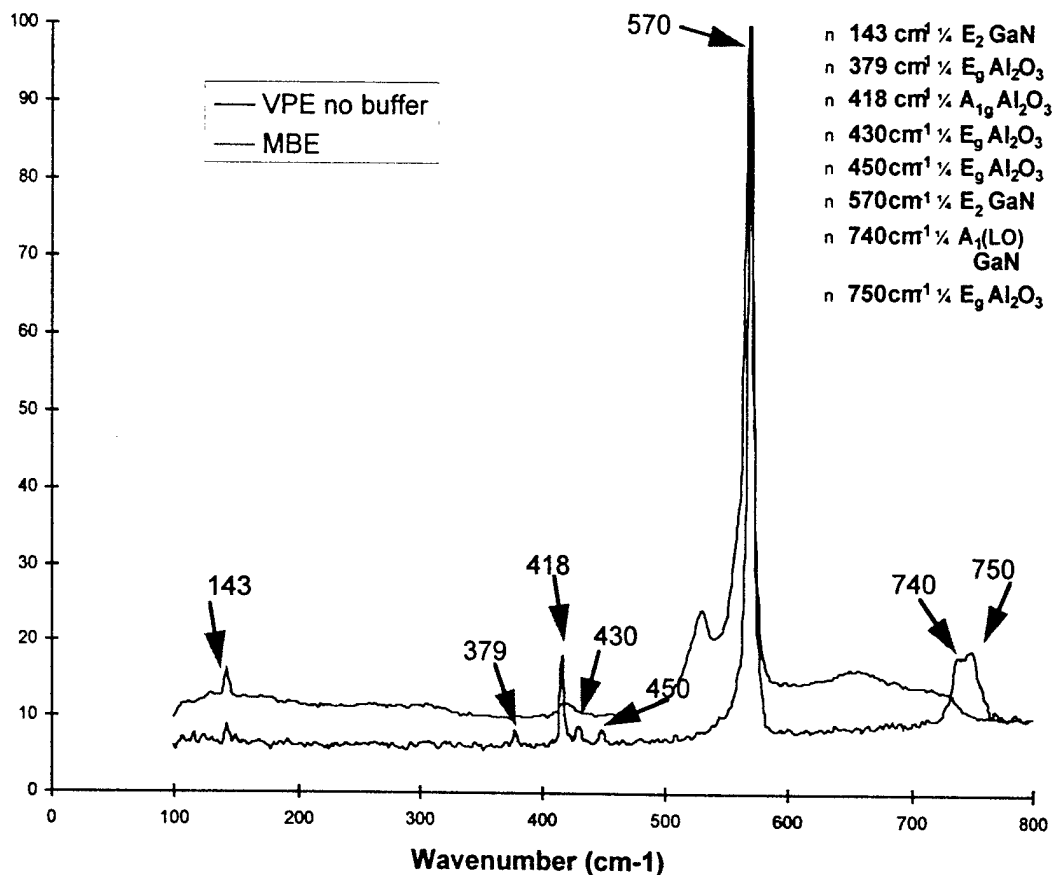


Figure 1: RAMAN measurement on GaN grown by MBE and VPE.

Variable temperature photoluminescence reveals the dominant defects through their characteristic emission bands. The ultimate goal is to correlate the small scale material defects with the electrical and optical properties of GaN films. We also now have the option of reducing the measurement spot size to $150 \times 200 \mu\text{m}^2$ and we are in the process of characterizing the new set-up. The microspot option will be very useful for the study of MOCVD grown samples which are more spatially inhomogeneous.

For the proper interpretation of cross-sectional AFM images, performed for the direct imaging of the GaN/ Al_2O_3 interface, it was concluded that it is necessary to polish out the breaking damage, as is done in TEM preparation of samples. Images of the surfaces of one of our high quality MBE samples from Siemens has revealed the presence of what might be quantum dots spontaneously induced by the high lattice mismatch of about 45 nm height. Such structures might prove to be very useful in realizing low threshold lasers.



Figure 2 : Surface of MBE GaN on Sapphire indicating the presence of 45 nm high GaN dots.

6. GaN Process Technology and Devices

The most common method of fabricating mirrors in semiconductor lasers is to cleave along parallel crystal facets. However, the surface of cleaved III-Ns on sapphire is rough because the epitaxial GaN does not follow the cleavage plane of the sapphire substrate. Thus, one of the goals of this project was to develop dry-etching techniques or mechanical polishing methods for the fabrication of vertical mirror facets as an alternative to cleaving processes. We have found that mechanical polishing of GaN on sapphire into bars using diamond grit leaves scratches and damage. This process is also not manufacturing oriented since laser bars must be processed individually. Fortunately, we have succeeded in etching vertical facets in GaN using a $\text{Cl}_2/\text{H}_2/\text{Ar}$ ECR dry-etching process.

Nakamura's first reported InGaN MQW laser relied on etched facet mirrors made by Cl_2 RIE. Our approach for obtaining high temperature etching is to rely on self-heating of the sample in the $\text{Cl}_2/\text{H}_2/\text{Ar}$ plasma. Ni is used as the etch mask, and an etch rate of $5270 \text{ \AA}/\text{min}$ is achieved. This rate is the highest yet reported for GaN, which we attribute predominantly to the self-heating of the sample during the etching. Figure 3. shows an SEM micrograph of the sidewall profile of a GaN sample etched to a total depth of $2.6 \text{ }\mu\text{m}$. The bottom $1.5 \text{ }\mu\text{m}$ of the facet is vertical, while the upper $1.1 \text{ }\mu\text{m}$ has an angle that is slightly less than vertical due to the erosion of the Ni mask. A maximum GaN to Ni etch selectivity of 16 is obtained, which makes this process suitable for laser mirror fabrication in GaN.

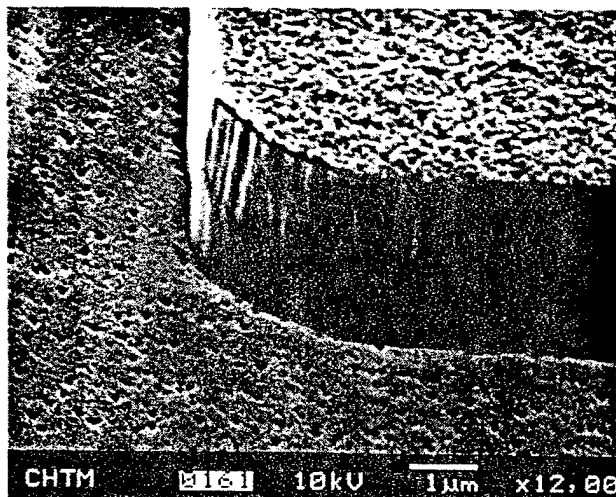


Figure 3: SEM micrograph of the sidewall profile of a GaN sample etched in $\text{Cl}_2/\text{H}_2/\text{Ar}$ ECR plasma. The conditions are 700 W microwave power, 10 $\text{Cl}_2/15 \text{ H}_2/9 \text{ Ar}$, 300 W RF power, -120 V DC bias, and 4 mTorr chamber pressure. The etch rate is 5270 Å/min. The GaN to Ni mask etch selectivity is 16. The bottom 1.5 µm smooth and vertical facet which corresponds to the first few minutes etching is large enough to provide sufficient feedback for lasing mode in GaN.

We have fabricated blue LEDs from UNM grown material consisting of a single $\text{In}_{0.22}\text{Ga}_{0.78}\text{N}$ quantum well with $\text{In}_{0.09}\text{Ga}_{0.91}\text{N}$ barriers sandwiched between p- (top) and n-type (bottom) GaN layers. The substrate material is sapphire. A schematic diagram of the layer structure is shown in Figure 4. The LEDs are made in a "lock and key" type of layout as shown in Figure 5 with the n-type GaN layer being accessed by etching a 0.6 µm deep mesa in Cl_2/H_2 RIE. The etch rate for this process was approximately 5500 Å/min. A Ti/Al metalization alloyed at 700 C was used for the n-type contact. The p-type ohmic contact is Pt/Au.

As seen in Figure 6, the peak of the electroluminescence spectrum is at 435 nm. The external quantum efficiency is 0.02%, most likely due to low p-type doping activation in the upper GaN layer. A plot of the optical power versus bias current is shown in Figure 7. The maximum power out is about 150 µW. We have measured the series resistance of the LEDs and determined the resistance is inversely proportional to the periphery of the device. From this result, we conclude that the light emission is coming predominantly from the edges of the metal contacts. The total series resistance is typically 11.5 W-mm and the ideality factor of the LEDs varies from 19-21 for leakage devices.

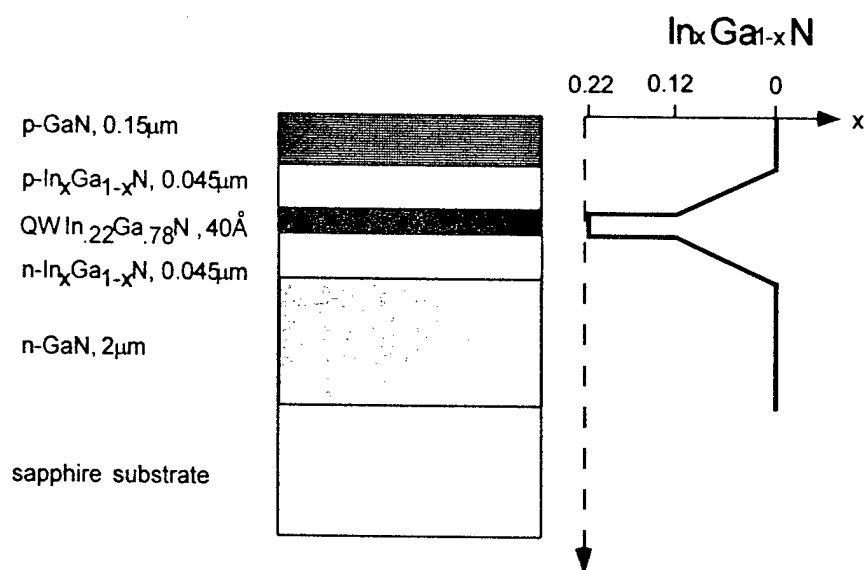


Figure 4. InGaN/GaN SQW LED layer structure grown by MOCVD on a sapphire substrate

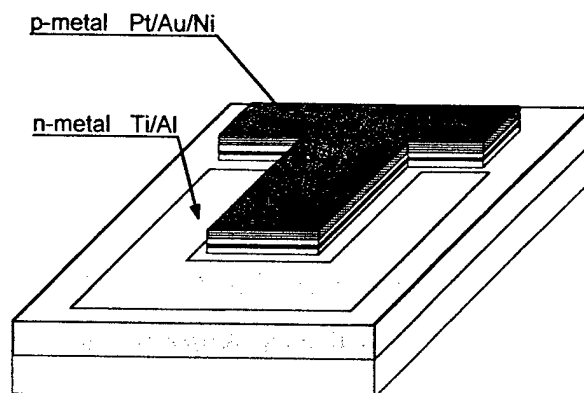


Figure 5. Schematic diagram of the simple LED device

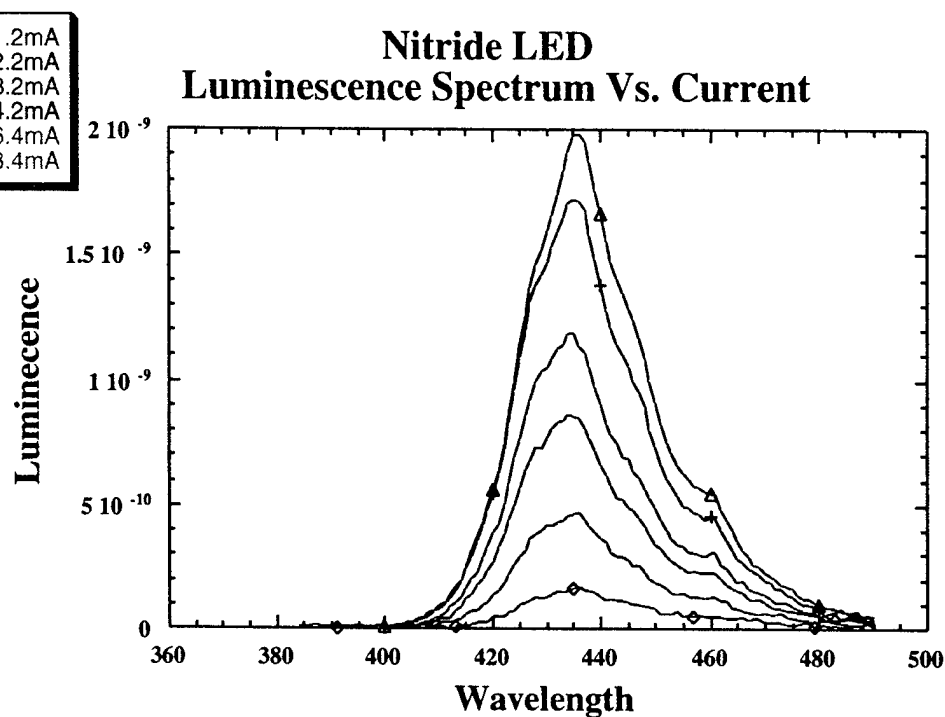


Figure 6. Electroluminescence spectra of an InGaN QW LED

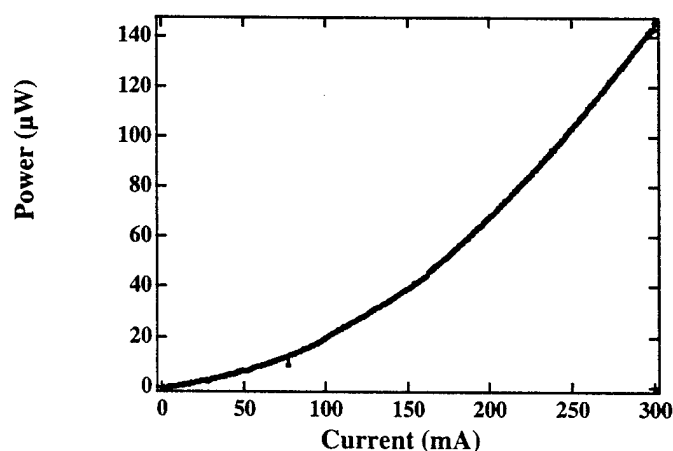


Figure 7. Light out as a function of bias current for an LED from wafer #264. The quantum efficiency is 0.02%.

We have performed ohmic contact studies on MOCVD-grown n- and p-type GaN using circular metal contacts as shown in Fig. 6 to avoid the need for isolation. On n-type GaN, we find that a non-alloyed ohmic contact with a specific contact resistance, r_c , of $1.0 \times 10^{-5} \text{ W-cm}^2$ is possible using a Ti/Al metalization. The tunneling ohmic contact is formed by annealing the bare GaN wafer at 1100 C in high-purity nitrogen before metalization. This process generates nitrogen vacancies that act as donors and make the surface heavily n-type.

To activate Mg acceptors in GaN, an anneal at 700 C for 20 minutes is typically used to drive out compensating hydrogen in MOCVD-grown material. Given our n-type contact results, we investigated whether the acceptor activation anneal degraded ohmic contacts to p-GaN by inadvertently causing dopant compensation at the surface due to nitrogen desorption. We compared the effect of different activation anneal techniques on the r_c of Ni/Au, Pd/Pt/Au, Pt/Au, and Pt metallizations to p-GaN grown by MOCVD. The p-GaN was activated either before or after metal deposition. The pre-metallization annealed samples were heated at 700 C for 20 min. face-down on an undoped GaN wafer, a p-GaN wafer, or left uncapped. For the samples that were not pre-metallization annealed, a 750 C, post-metallization heat treatment performed on all wafers simultaneously activated the dopant and alloyed the metal. We found that the hydrogen had no difficulty in escaping through any of the metallizations at 750 C.

Although annealing the contacts improves their ohmic behavior, all exhibit a slight bend in their room-temperature I-V characteristic near the origin. Thus, it is necessary to define the current at which r_c is measured. Table 1 compares the r_c of metal contacts to GaN that use the different pre-metallization anneal treatments. The hole concentration is about $1 \times 10^{17} \text{ cm}^{-3}$, and r_c is measured at 10 mA. There is no significant difference in r_c among samples that use the pre-metallization anneal with the different capping options. However, a lower r_c is obtained for samples that are annealed only after metallization. Presumably, the good contact between GaN and metal prevents nitrogen desorption and the resultant compensation at the surface of GaN.

As seen from the data in Table 1, r_c varies little as a function of the metallization for a given process. Table 2 examines this phenomenon more closely by including Ti in a study of ohmic contacts to p-GaN with a hole concentration of about $2 \times 10^{17} \text{ cm}^{-3}$. The results show that there is no obvious trend in r_c with the metal work function, indicating that the Fermi level is pinned for this moderate hole concentration. Finally, we note that pinning of E_F at the surface dampens the effect of nitrogen desorption during the activation anneal. At higher hole concentrations for which E_F is not as strongly pinned, the difference in r_c between ohmic contacts that employ the pre-metallization anneal or only the post metallization anneal will become more apparent.

Studies of the electrical properties of the Pt/Au contacts reveal that the sheet resistance and the r_c show a temperature dependence, which could prove important for high temperature device applications. With increasing temperature, it is found that the sheet resistance and the r_c decrease and that the I-V linearity of the metal contacts improves significantly. From 25 C to 285 C, the sheet resistance decreases by an order of magnitude, from 64,000 to 6,070 Ω/Square . At room temperature, a slightly rectifying I-V characteristic curve is obtained, while at 245 C and above, the I-V curve is linear. A specific contact resistance of $6.6 \times 10^{-4} \Omega\text{-cm}^2$ for the Pt/Au was obtained at a temperature of 285 C. This result is the lowest reported r_c for ohmic contacts to p-GaN. The significant decrease in the r_c at higher temperature is attributed to an increased hole concentration which results in more efficient tunneling through the voltage barrier at the metal/GaN interface. The improvement in I-V linearity with increasing temperature indicates a transition from current flow that has a significant thermionic component at low Torr to one that is dominated by tunneling at high Torr.

6.1 Process & Device Summary

1. Etch rates of GaN as high as 660 Å/min demonstrated using hydrogen-free plasma etching in SiCl₄/Ar mixtures. This process is suitable for steps where reasonable etch rates are desired and hydrogen compensation must be avoided, such as the etching of p-type GaN.
2. Highest etch rate ever reported for GaN, 5270 Å/min.
3. Non-alloyed Ti/Al ohmic contacts to n-type GaN achieved with a specific contact resistance as low as 1×10^{-5} W-cm² using a high-temperature anneal 1120 C prior to the metallization to desorb nitrogen.
4. Fabrication of an InGaN quantum well blue LED with 150 μW output power.
5. Ohmic contact to p-GaN with specific contact resistance as low as 6.6×10^{-4} Ω-cm².

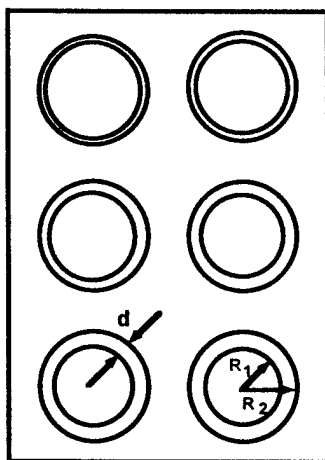


Figure 8. A diagram of the circular contact layout showing important parameters. For this work, the outer contact radius, R_2 , is 200 μm, and the gap spacing, d , is varied from 5 to 45 μm.

Table 1. The r_c of ohmic contacts to p-GaN for various metallizations and different pre-metallization anneal treatments. The r_c was measured at a current of 10 mA. All samples were given a 750 C post-metallization anneal for 10 minutes.

Sample	Metals	Pre-metal anneal?	r_c ($\text{W}\cdot\text{cm}^2$)
308C	Pt/Au	No	1.9×10^{-3}
308A	Pt/Au	Yes, u-GaN cap	5.3×10^{-3}
308I	Pt/Au	Yes, p-GaN cap	2.6×10^{-3}
308K	Pt/Au	Yes, Uncapped	3.2×10^{-3}
308G	Pt	No	1.4×10^{-3}
308F	Pt	Yes, u-GaN cap	7.6×10^{-3}
308J	Ni/Au	No	3.3×10^{-3}
308B	Ni/Au	Yes, u-GaN cap	5.5×10^{-3}
308E	Pd/Pt/Au	No	2.4×10^{-3}
308D	Pd/Pt/Au	Yes, u-GaN cap	7.4×10^{-3}

Table 2. A comparison of the specific contact resistance for different metal contacts to p-GaN. There is no obvious trend in r_c with the metal work function. The electron affinity of GaN is 4.1 eV.

Sample	Metal	Work Function (eV)	r_c ($\text{W}\cdot\text{cm}^2$)
309E	Pt	5.65	4.3×10^{-3}
309C	Ni	5.15	2.1×10^{-3}
309B	Pd	5.12	8.0×10^{-3}
309A	Au	5.10	6.2×10^{-3}
309D	Ti	4.26	2.5×10^{-2}

7. Ion Etching of Nitrides

GaN and its alloy nitrides (InGaN and AlGaN) are leading candidates for the development of optoelectronic devices operating in the green to UV. This has generated intensive effort in the growth, processing and characterization of these materials. In order to realize device applications of these materials, a reliable etching technology must be established. Although hot phosphoric acid and sodium hydroxide solution slightly etch GaN, it is almost impossible to transfer fine patterns to GaN films by any wet chemical etch due to the chemical stability of GaN.

Reactive ion etching using chlorine-containing gases is a promising method for etching GaN. Several research groups have reported the reactive ion etching or ECR plasma etching of GaN and its alloy nitrides using SiCl_4 , BCl_3 , C_2ClF_5 and Cl_2 . Hydrogen-containing gases like CH_4 and HBr have also been used to etch GaN. For reactive ion etching, both chemical reactions with reactive neutral species and physical sputtering by accelerated ion species contribute to the etching process. In this paper, we report the reactive ion etching of GaN using trifluoromethane (CHF_3) and chloropentafluoroethane (C_2ClF_5) gases. Both gases are not flammable and less toxic and corrosive than typically used gases for GaN etching.

GaN films were grown by electron cyclotron resonance (ECR) plasma assisted MBE on semi-insulating (100) GaAs and (0001) sapphire substrates. Elemental Ga and a nitrogen plasma were used as source materials. Characterization of the GaN films by X-ray diffraction, Raman spectroscopy and cross-sectional transmission electron microscopy showed that the GaN films had the wurtzite structure. The films grown on (100) GaAs consisted of columnar domains, oriented with the c-axis normal to the surface.

GaN films with a thickness of 0.6 to 0.9 μm were patterned with positive photoresist, and etched using a Drytek model DRIE-184 reactive ion etching system. CHF_3 and C_2ClF_5 gases were introduced into the RIE chamber and Ar gas was added in order to stabilize the plasma discharge and enhance the etching anisotropy by increasing the non-reactive ion bombardment. The RF plasma power was varied between 100W and 500W and the pressure varied between 60 - 300 mTorr. CHF_3 or C_2ClF_5 flow rates were varied between 20 and 50 sccm. After etching, the remaining photoresist was removed by an oxygen plasma and $\text{H}_2\text{SO}_4:\text{H}_2\text{O}_2$ (1:3) solution. Etch rates were measured by profilometry.

The effect of RF plasma power and chamber pressure on the etch rate are shown in Figure 9. Etch rates were proportional to the ratio of plasma power (W) to pressure (mTorr). As the pressure is reduced, the plasma sheath thickness and the voltage across the sheath increases. The plasma potential thus increases, as does the ion bombardment energy. In this regime, the physical etching process plays a major role. At higher pressure, chemical etching by reactive neutral species dominates. According to scanning electron microscopy, etch pits were observed only in the high-pressure etched samples. The concentration of etch pits was in the range of $10^8/\text{cm}^2$. The higher etch rate at lower pressure implies that the physical etching process dominates the GaN etch rate. At higher RF plasma power, the dissociation efficiency increases, and etching species becomes more energetic, thus the etch rate increases with higher plasma power. The etch rates were only slightly affected by the crystalline quality of GaN film. The etch rate of the single crystalline GaN film on (0001) sapphire is approximately 15% lower than that of the domain-structured GaN film on (100) GaAs.

The surface morphologies of etched and unetched GaN films grown under identical conditions were examined by atomic force microscopy (AFM). $3\mu\text{m} \times 3\mu\text{m}$ areas of the film surface were scanned. The unetched film has a root mean square (RMS) roughness of 17.548 nm, while the RMS roughness of the reactive ion etched film is only 12.607 nm. This implies that the surface is certainly not roughened by the etching process and may actually be smoother with more rapid etching of the peaks of the film. Fine pattern transferring into GaN films by using $\text{C}_2\text{ClF}_5/\text{Ar}$ and CHF_3/Ar plasmas was successful.

Focus Area: Diode-based Visible Sources**Task Quasi-phasematched Second Harmonic Generation**
(415-725-2160, fejer@ee.stanford.edu)**Personnel**

M. M. Fejer (PI)

J. L. Hoyt

R. Jain

J. Walpole

Summary

The goal of this task is to develop robust, diode-laser-based sources of coherent visible and UV radiation, based on second harmonic generation (SHG) of infrared input radiation. The motivation for this work is applications such as sensors, biomedical instrumentation, and displays, requiring solid-state sources of coherent UV/VIS radiation in the near term. Together with the long lead time (five years in recent estimates from Nichia Chemicals) for the availability of GaN diode lasers, interest in UV wavelengths shorter than are likely to be accessible in GaN lasers, and the difficulty in scaling even infrared diffraction-limited diodes to powers exceeding 1 W, approaches based on frequency conversion of IR diode lasers and diode-pumped solid-state lasers are appealing. Requirements on the sources range from sub-mW, highly coherent (less than 10 MHz) sources for spectroscopic sensors, to > 1 W of red, green, and blue for three-color displays. Our baseline approach for VIS/UV generation uses quasi-phasematching (QPM) in periodically-poled lithium niobate (PPLN) channel waveguides. Variants investigated include planar waveguide and bulk geometries, QPM in other ferroelectric crystals, and growth of patterned-orientation films of II-VI semiconductors for monolithically integrable versions of these devices. A major component of the program is development of high power, single-mode diode lasers as pump sources for these devices.

Waveguide devices have been demonstrated in our laboratory producing 5 mW blue output and at industrial laboratories as much as 100 mW output with a diode-laser pump. We have also demonstrated bulk single-pass devices generating greater than 2 W in the green with a diode-pumped solid-state laser pump. The practical utility of such devices depends on several key issues, including appropriate pump sources, conversion efficiency, reproducible fabrication processes, coupling of the waveguide to the diode laser, wavelength and temperature acceptance bandwidths, and lifetime-limiting phenomena. Our efforts have been directed at addressing these practical issues, and important results have been obtained in these areas.

SHG Conversion Efficiency

The efficiency of these devices depends on the overlap of the waveguide modes with the domain inverted region, and on the square of the length of the device. We have developed electric-field poling technology to replace the shallow titanium diffusion poling technology used previously (which limited efficiency to about 10% of theoretical maximum). Resulting domain gratings penetrate through the entire thickness of 0.5 mm thick substrates. Performance of long pitch ($> 10 \mu\text{m}$) gratings is nearly at the ideal limit; this technology has been transferred to two

companies. The shorter pitch ($< 6 \mu\text{m}$) gratings necessary for visible light generation are more difficult to fabricate, but have recently been demonstrated and are now being tested for optical applications. As much as 2.5 W of 532 nm radiation was generated in bulk electric-field-poled samples; waveguide devices are currently being tested.

We have also investigated processes that limit the useful length of these devices. We have developed models for the ion exchange and annealing processes involved, setting fabrication tolerances, and engineered the thermal and chemical processing conditions to reliably produce 3 cm long IR devices with nearly ideal behavior, with an order of magnitude higher efficiencies than previous 1 cm devices. Together with the deep electric-field poled domains, these processing improvements greatly increase the yields of high-quality devices.

Coupling to Diode Lasers

The key issue in coupling a diode laser to an SHG waveguide is difficulty in stably launching the output of the diode into the small ($2 \mu\text{m}$) waveguide mode. We have developed adiabatic waveguide tapers that allow expansion and compression of mode diameters by a factor in excess of 20 (observed input diameters over $40 \mu\text{m}$ for waveguide with a $2 \mu\text{m}$ mode diameter), greatly easing the necessary alignment accuracy. These tapers, based on periodically segmented waveguides created by diffusion through a segmented mask, are backward compatible with existing waveguide. These tapers are likely to be applicable to other problems in guided wave devices, such as fiber pigtailling of electrooptic modulators for telecommunications systems.

A second issue in coupling to diode lasers is matching the diode wavelength to the narrow acceptance bandwidth (0.1 nm typically) of the SHG device. The bandwidth is inversely proportional to the length, so that a tradeoff exists between efficiency and bandwidth. In addition to the increase in bandwidth (at fixed efficiency) that accompanies the shorter devices enabled by improved poling and processing, we have demonstrated spread spectrum schemes based on aperiodic domain gratings that enable an order of magnitude increase in gain-bandwidth product over simple periodic gratings. New designs based on super-Gaussian apodization reduce pass-band ripple over earlier Barker code designs. Bandwidths of 1 - 2 nm with acceptable conversion efficiencies appear feasible.

Lifetime Limiting Effects

While useful output powers in the blue spectral range have been demonstrated in QPM channel waveguide devices, observed lifetimes have varied erratically. The underlying effects are complicated and not well characterized, and depend on several parameters, including power, wavelength, material and processing, domain structure, temperature, etc. We have developed a model for optogalvanic effects in bulk periodically-poled ferroelectrics, which quantifies the strong dependence of the optical effects on the duty cycle of the domain grating, consistent with the variability in observed photorefraction. We also have measured the photorefraction in channel waveguides with a pump-probe technique, which showed that a previously unobserved two-color effect (perturbation depends on simultaneous presence of IR and UV radiation) dominates the photorefraction under typical conditions in Ti-poled waveguides. The two-color effect appears less important in electric-field-poled waveguides, but the processes involved are

not yet completely elucidated. There appear also to be effects related to the oxidation state of native defects and impurities, which are altered as a consequence of the wafer patterning process. We are investigating post-fabrication processing, e.g. reactive atmosphere processing, for which preliminary results indicate substantially reduced sensitivity to photorefractive effects. Given our results, as well as industry demonstrations of high power devices, these lifetime issues are expected not to be a limiting issue in future devices.

Other Materials

We have also investigated materials other than periodically-poled lithium niobate for SHG applications. One effort has been directed at lithium tantalate, which has similar optical and ferroelectric properties to lithium niobate, and a UV absorption edge at 280 nm compared to 350 nm in lithium niobate, permitting operation farther into the UV. It has also proven to be easier to fabricate fine-pitch domain gratings in lithium tantalate, with structures down to 1.75 μm already observed.

Fine pitch poling of lithium tantalate has continued with a quarter-wafer process yielding 15 - 25 mm long samples suitable for visible and UV generation. So far, device-test samples have been fabricated with grating periods of 7.5, 6.0, 5.5, 3.37 and 2.6 μm . Efficient second harmonic generation in the visible has been demonstrated (with the 7.5 μm pitch device) and a number of UV wavelengths have been generated from first, second and third order QPM processes. Up to .3 mW of 393 nm UV radiation have been generated, and the existing crystals have the potential for generating even shorter wavelengths down to the band edge of LiTaO_3 , near 280 nm by utilizing higher order QPM, e.g. we have generated 325 nm light, useful for copper vapor sensing, by SHG of 650 nm light from a diode laser. Preliminary fabrication studies have been carried out on 1.75 micron period gratings. Though the domain quality of these fine pitch gratings still needs improvement, our initial results were encouraging and further development is planned.

We are investigating the use of II-VI semiconductors (CdTe, ZnTe and ZnSe) for QPM SHG, because their large SHG coefficients, optical transparency, and compatibility with GaAs substrates. QPM is accomplished by a periodic change in the crystal orientation, established by a patterned $\langle 111 \rangle / \langle 100 \rangle$ CdTe layer on GaAs. This serves as a template for subsequently grown ZnTe/ZnSe waveguides. During the first generation of OMC funding we developed the patterning technology of the CdTe template, including a low-temperature in-situ preparation for epitaxial regrowth. We then optimized our growth conditions for good quality ZnSe and ZnTe waveguide layers. A typical waveguide, which was targeted to have a core thickness of 1.5 microns and a 1 micron cladding layer, was grown on unpatterned GaAs, and planar modes were observed through a 1 cm long sample. Growth on the CdTe orientation templates of patterned ZnSe and ZnTe/ZnSe multilayered structures proved difficult due to the faceted growth on the exposed ridges of $\langle 100 \rangle$ CdTe, so we have developed an alternative approach. The new devices are redesigned to have an unpatterned $\langle 100 \rangle$ ZnSe cladding layer and a patterned ZnTe core. The growth conditions were optimized for growing $\langle 111 \rangle$ CdTe on $\langle 100 \rangle$ ZnSe by atmospheric pressure MOCVD. The device is made by growing the ZnSe cladding layer and 500 Å of $\langle 111 \rangle$ CdTe, then etching the CdTe in selected areas and regrowing the ZnTe core, which is $\langle 111 \rangle$ oriented in the masked regions and $\langle 100 \rangle$ where the CdTe was etched away. These layers

showed a very smooth core/cladding interface, but the top surface developed triangular ridges over the $\langle 111 \rangle$ areas. After a mechanical polishing step to smooth the top surface of the device waveguide modes were observed through the patterned waveguide indicating adequate quality of the patterned film for waveguide operation. Thus the full device is very nearly complete, although further improvement of the film uniformity, particularly at the boundaries between $\langle 111 \rangle$ and $\langle 100 \rangle$ regions, may be required for useful device performance. SHG testing of these devices is planned in coming weeks.

Application to Sensing

The quality of the SHG devices already demonstrated has been adequate for applications in atomic-absorption spectroscopic sensors for process control in physical vapor deposition of metals. Demonstrated applications include monitoring of Ti evaporation for synthesis of refractory alloys, and evaporated and sputtered Al, accomplished with external-cavity diode lasers doubled into the 390 nm range with QPM waveguides. This work was carried out in collaboration with New Focus, Inc.

Conclusion

Significant progress has been attained in the materials and device technologies associated with generation of coherent visible and UV radiation. Improved poling technology in lithium niobate has been developed based on electric-field poling with periodic electrodes, allowing improved efficiency and reproducibility of waveguide devices and also QPM bulk interactions. Adiabatically tapered waveguides have been developed using a periodic segmentation technique, allowing >20-fold mode size expansion at the input of a single-mode waveguide, significantly easing the tight coupling tolerances previously associated with these devices. New materials have been developed, including periodically-poled lithium tantalate, allowing extension of QPM techniques further into the UV (325 nm demonstrated, 280 nm potential), and orientation patterned II-VI semiconductors for future integration of nonlinear devices on GaAs substrates.

For applications requiring low powers and highly coherent radiation, i.e., spectroscopic process control sensors, the performance of direct diode-laser frequency doublers in the near-UV is already adequate, and devices are appearing in field applications. Devices generating diffraction limited visible radiation at powers exceeding 2 W, beyond currently available diode laser technology even in the IR, have been obtained with single-pass QPM SHG in PPLN, using diode-laser-pumped solid-state laser pump sources. Both these classes of sources are subjects of active industrial development today. Intermediate powers (5 mW in our laboratory, >100 mW in industry) have also been obtained by direct doubling of diode lasers. The technology of these latter devices, especially the requisite control of the diode laser spectrum, while readily demonstrated in the laboratory, remain challenging technological issues for commercial development. While the high-coherence low-power devices, and the high-power devices seem likely to remain superior to GaN technology for the foreseeable future, in intermediate-power applications with no spectral control requirements, e.g. optical data storage, GaN technology seems likely to be the most viable technology within the next several years (assuming solution of relevant materials issues), especially in areas where low cost rather than high performance is the driving consideration.

Focus Area: Optoelectronic Tools for Intelligent Manufacturing
Task: Monolithic Tunable Semiconductor Lasers
(415) 723-9775, Harris@Snowmass.Stanford.edu

Personnel

J. S. Harris (PI)
F. Sugihwo
M. C. Larson
A. Massengale

Significant Results

Space, time, and wavelength division multiplexing are currently pursued either independently or concurrently as means of increasing data transmission through optical fibers. Due to its ability to offer all of these multiplexing schemes, monolithically-fabricated wavelength-tunable diode laser is projected to play an important roles in the rapidly expanding area of optical communications. Additionally, tunable laser diode is potentially useful for frequency-modulation (FM) spectroscopic remote sensing which offers significant signal to noise ratio improvement or sensitivity, over conventional amplitude-modulation (AM) sensing.

Although a tunable edge-emitting laser has demonstrated tuning range as wide as 114 nm ($\Delta\lambda/\lambda \sim 7\%$) with sophisticated filter design, the truly continuous tuning range is limited to $< 1\%$. This is a natural consequence of long cavity length in edge-emitting lasers which results in short axial mode spacing. Mode-hopping occurs when the lasing wavelength is tuned beyond the axial mode spacing, $D\lambda_{ax}$. Vertical-cavity surface-emitting laser (VCSEL), on the other hand, has a short cavity length, on the order of the active wavelength itself. The short cavity length results in an axial mode spacing ($D\lambda_{ax}/l$) as large as $\sim 10\%$ or 100 nm in the near IR. Broad-range wavelength tuning without mode hopping is therefore possible simply through direct tuning of the optical path length of the cavity. Changing this length through refractive index modulation was limited to approximately 1%. Alternatively, the physical length of the cavity can be adjusted microelectromechanically through the use of a movable micro-mirror to achieve a much wider wavelength range. Using physical cavity length modulation, continuous tuning as wide as 4% was achieved in a vertical cavity light emitting diode, as well as 1.8% in a VCSEL. Recently, we demonstrate laser oscillation without mode hopping over a continuous wavelength range of 2.0 %--to our knowledge, the largest to date in any monolithically-fabricated diode laser.

The device is shown schematically in Figure 9. The bottom mirror is a 22.5 period GaAs/AlAs distributed Bragg reflector (DBR) with a center wavelength λ_0 near 970 nm. The $\text{In}_{0.2}\text{Ga}_{0.8}\text{As}$ cavity contains an active region made up of two 6 nm $\text{In}_{0.2}\text{Ga}_{0.8}\text{As}$ quantum wells placed within the intrinsic region of a *p-i-n* diode. The deformable membrane top mirror is made up of a quarter wavelength layer of GaAs, $\text{SiO}_2/\text{SiN}_x/\text{SiO}_2$ DBR layers, and Au reflector/electrode. The mirror consists of a central reflector held by four tensile-strained legs attached to four rigid contact pads suspended above the semiconductor cavity, producing an air gap whose thickness can be adjusted by applying voltage bias between the membrane and *p*-layer. The air gap is fabricated through the selective wet chemical etching of an $\text{Al}_{0.85}\text{Ga}_{0.15}\text{As}$ sacrificial layer, whose

thickness of $0.85 \mu\text{m}$ is slightly larger than $3\lambda_0/4$, because electrostatic force is only attractive in nature. A current blocking layer formed through the selective lateral oxidation of AlAs limits current injection from the four p -cavity contact fingers and n -DBR to a non-oxidized aperture directly underneath the central reflector.

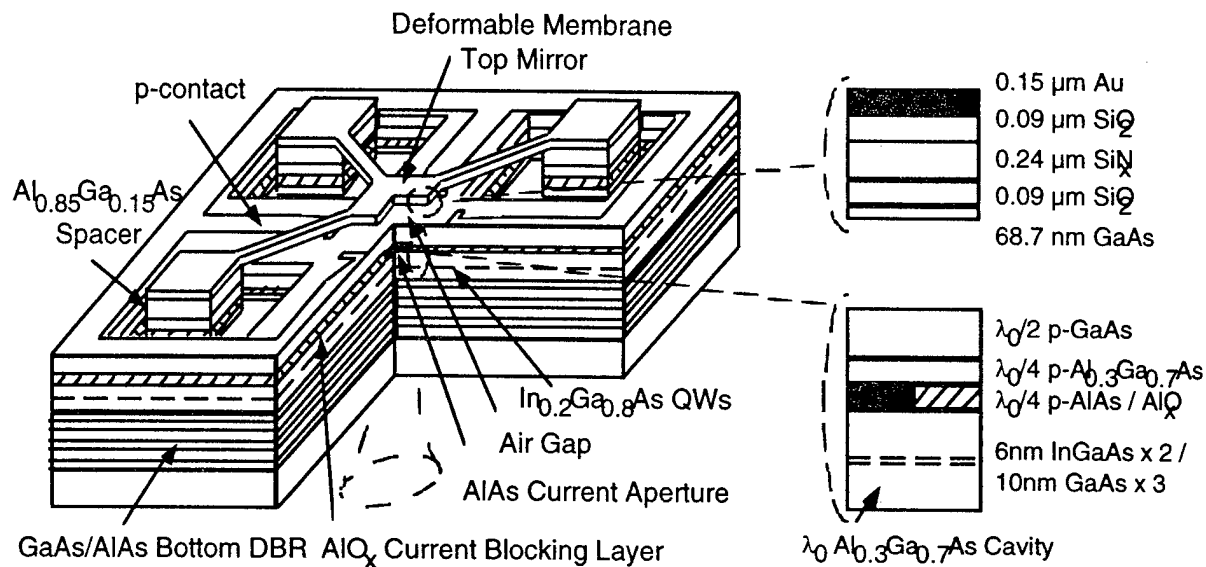


Figure 9. Schematic diagram of the micromechanical tunable VCSEL. Inset is the layer structure of the deformable membrane mirror and the semiconductor cavity/active layers.

Devices with central reflector sizes of 20 and $30 \mu\text{m}$ were biased for continuous wave (CW) operation at room temperature without heat sinking, and light was collected through the transparent GaAs substrate. Aperture diameters of approximately $5 \mu\text{m}$ typically resulted in threshold currents in the range of 0.4-0.6 mA. Figure 10 shows a plot of power output and voltage vs. current. For this device, the threshold current was 0.34 mA, and the slope efficiency was 0.083 W/A, yielding a differential quantum efficiency of 6.5 %. This represents approximately a factor of 10 improvement compared to earlier designs in which the semiconductor cavity layer was directly adjacent to the air gap. Further increases in efficiency should be possible simply by decreasing the reflectivity of the bottom DBR, since its output coupling--predicted to be less than 0.15%--is quite low compared to other optical losses present in the membrane or air gap.

Figure 11 shows the superimposed output spectra at various membrane tuning voltages from a device with a minimum threshold current of 0.4 mA, operated at a constant diode current of 0.5 mA. The spectra indicate predominantly fundamental transverse mode operation with a mode suppression ratio of ~ 24 dB. The lasing wavelength shifted continuously from 968.2 nm at 0V tuning bias to 949.1 nm at 17.8V, for a total range of 19.1 nm. The threshold current and output power remain relatively constant over much of this range, deviating only at shorter wavelengths. This is likely a result of tuning near the short wavelength edge of the gain spectrum. Since an error in layer thickness of approximately -1% resulted in the tuning range being centered instead near 960 nm, we believe an even wider range would otherwise be possible.

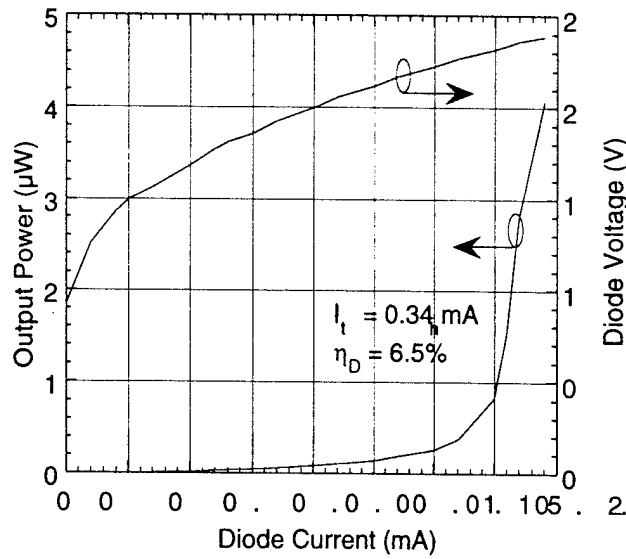


Figure 10. Output power and diode voltage vs. Diode current at 0V tuning bias

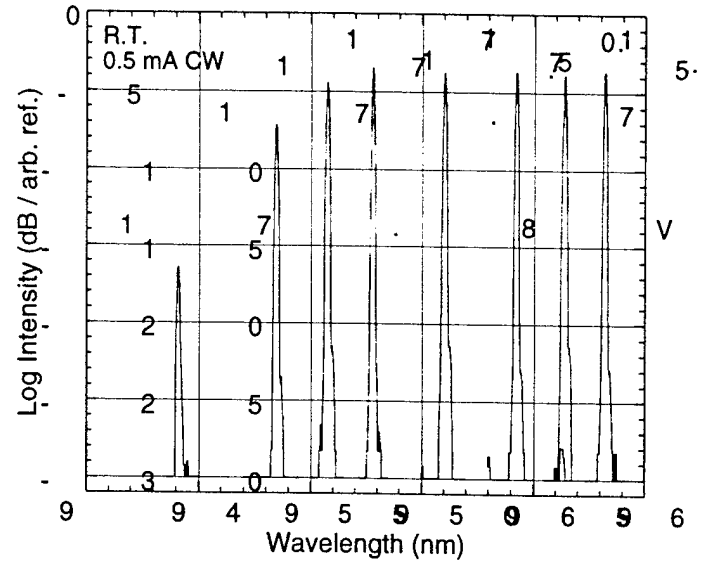


Figure 11. Superimposed lasing spectra at a constant diode current of 5 mA and various membrane-p tuning voltages

Focus Area: Optoelectronic Tools for Intelligent Manufacturing**Task: Real-time feedback control for semiconductor processing
(415)723-9775, Harris@Snowmass.Stanford.edu)****Personnel**

J. S. Harris (PI)

R. N. Zare (PI-Chemistry)

J. Martin

B. A. Paldus

Significant Results

Prior reports focused upon the development of cavity ring down spectroscopy (CRDS) for significantly improving detection of micro-contaminants in semiconductor processing. This final report focuses upon refinement of the technique to utilize a semiconductor laser and thus move significantly toward a practical system for routine feedback control of semiconductor processes. As traditionally practiced, absorption spectroscopy is limited in sensitivity to approximately one part per ten thousand ($1:10^4$) to one part per hundred thousand ($1:10^5$). This limitation arises from instabilities in the intensity of the light source that are translated into noise in the absorption signal. CRDS is a new spectroscopic method for making absorption measurements with increased sensitivity, on the order of one part per ten million ($1:10^7$) to one part per billion ($1:10^9$), or even higher. This feat is accomplished by surrounding the absorbing material by an optical resonator, normally consisting of two highly reflecting mirrors. A light pulse is directed onto one mirror and the light transmitted through that first mirror circulates in the optical cavity bouncing back and forth between the two mirrors. The stored radiant energy decreases in time, i.e., "rings down."

For an empty cavity the ring-down time obeys exponential decay with a ring-down lifetime that depends only on the reflectivity of the mirrors, the mirror separation, and the speed of light in the cavity. When the wavelength of the incident light pulse is tuned to an absorption feature of the medium inside the optical cavity, the ring-down is increased. Under suitable conditions the time rate of change of the ring-down is almost perfectly exponential so that a ring-down time can be defined. An absorption spectrum is obtained by plotting the reciprocal of the ring-down time versus the wavelength of the incident light. The advantage of CRDS is not only in increased pathlength caused by multiple reflections, but, more importantly, an insensitivity to the amplitude of the light pulse. In other words, the intensity fluctuations of the light source become no longer the limiting feature in making sensitive absorption measurements.

CRDS has been applied to numerous systems in the visible and has recently been extended into the infrared. The infrared region is particularly appealing because molecules are so readily identified using what is called the "infrared fingerprint region." For that purpose, the ideal light source might be a tunable infrared diode laser because of its compactness, low cost, durability, high wallplug efficiency, and compatibility with optical fiber technology for remote sensing. As laser diodes are becoming available over the entire spectrum thanks to new materials systems such as Gallium Nitride, laser diodes are, in fact, expected to become the general light source of choice from the ultraviolet into the infrared.

One of the serious problems for diode lasers is that of optical feedback from the ring-down cavity into the laser diode. In order to overcome this problem, we investigated a scheme previously demonstrated by Martin and used to stabilize laser diodes, in the context of CRDS. An acousto-optic modulator (AOM) is placed between the laser diode source and the optical cavity.

From our earlier work, it is clear that diode lasers are very sensitive to optical feedback, even at levels below -80 dB. The effects of feedback on laser behavior vary widely, and can range from line narrowing or broadening to spontaneous mode hopping, or even to "coherence collapse." In the weak feedback regimes, the laser remains sensitive not only to the power level but also to the phase of the returning light. Hence, the length of any external cavities coupled to the laser becomes critical. The effect of the AOM frequency shift in the returning light is to force the diode laser to cycle through all values of phase with a period equal to the reciprocal of the frequency shift. This phase cycling then directly determines the laser linewidth.

By introducing an AOM into the external cavity, the light that is fed back is frequency shifted, which has the effect of averaging over its phase, which stabilizes the time-averaged behavior of the diode. This stabilization thereby eliminates the necessity of maintaining an extremely stable external-cavity length and we have shown that AOMs can provide control of the time-averaged spectral width of the output light over about two orders of feedback magnitude, which permits free-running laser diodes to be operated with stable linewidths ranging from 7 to 200 MHz.

The placement of an AOM between the RDC and the laser diode source has allowed us to exploit feedback stabilization of the laser diode source so that we are able to perform CRDS. We have focused upon detection of water vapor in ambient laboratory air for this demonstration. In this spectrum, the weakest peak detectable was at 831.605 nm with a linestrength of 2.1×10^{-24} cm²/molecule for a water concentration of 10 parts per thousand. The baseline signal-to-noise ratio of the peak was in fact 10. The temporal resolution of the ring-down time constant was 0.6% for an average baseline noise of 20 ns on an average baseline ring-down constant of 3000 ns. Furthermore, we had such a strong signal on the detector that we could not make full use of the averaging capabilities of our electronics because the counting bins would saturate.

The mirrors employed were nearly optimal for ring-down because they had a reflectivity of 99.93%. Finally, the diode laser frequency at 830 nm was not optimal for studying water vapor because absorption strengths 10^4 times greater are found at 1.3647 μ m. Hence, the construction of an identical system optimized to detect water vapor in trace amounts at levels of one part per billion is not difficult to imagine, based on an extrapolation of our present results. By using very sensitive low-noise detectors such as avalanche photodiodes in the infrared where photomultipliers are not readily available, and using a multichannel scalar to count photon statistics rather than electronics to detect the output waveform directly.

In this scheme, the AOM not only switches the light source on and off in a controllable manner with potentially steep rise/fall times (commercial AOM's with 5 ns rise/fall times are currently available), but provides additional stabilization of the laser diode linewidth (or frequency noise) in a controllable manner, which depends on the amount of light fed back from the zeroth and first orders of the AOM. Hence, the requirements for a stabilized, external cavity or distributed

feedback diode laser are relaxed. Furthermore, our use of a wider bandwidth pulse allows overlap with several cavity modes with the laser source frequency spectrum, which not only improves the shot-to-shot fluctuations in energy transmitted by or built up inside the cavity but allows us to keep our cavity length constant. This feature greatly reduces mechanical instabilities and wear for long-term reliability of the device.

By using a photon-counting photomultiplier tube or avalanche photodiode and multichannel scalar to detect and fit our output signal, we can make use of very high reflectivity mirrors while maintaining an equivalent signal detection signal-to-noise ratio. The advantage of using photon-counting is that high photon fluxes are undesirable because they overload the discriminator, so that for the optimal photon fluxes derived for a typical multichannel scalar (10^6 - 10^7 photons/sec), for a typical commercial unstabilized laser diode of 20-50 mW, we can use mirrors having $R=99.995\%$ in the near-infrared. Hence, we anticipate that can achieve sensitivities of parts per billion.

Focus Area: Optoelectronic Tools for Intelligent Manufacturing**Task: Frequency Agile Diode Lasers****(505-277-0768, luke@chtm.eece.unm.edu)****Personnel**

L. F. Lester (PI)

Significant Results

We have fabricated widely-tunable, low threshold current laser diodes from an engineered multiple quantum well gain structure consisting of three compressively strained $\text{In}_{0.2}\text{Ga}_{0.8}\text{As}$ wells of different thicknesses. Using a grating in an external cavity, a continuous-wave tuning range of 70 nm (911-981 nm) is measured for a 155- μm semiconductor cavity length device at a current of 32 mA. This is the lowest reported bias current for a semiconductor laser with this broad a tuning range. A maximum continuous wave tuning of 80 nm (901-981 nm) has been measured at a bias current of 95 mA. At long wavelengths, we have observed a suppression of amplified spontaneous emission and preferential population of the lowest energy well. Ideally, a tunable semiconductor laser should have minimal threshold current and output power variation across a broad wavelength range of operation. Quantum well (QW) materials offer low threshold currents coupled with a broad tuning range, as well as the ability to tailor the gain medium to a specific wavelength range. Past work on broadly tunable quantum well laser diodes has focused on materials which contain either multiple identical wells or stepped quantum wells.

We have investigated an alternative multiple quantum well (MQW) approach, in which the transition energies from the first conduction to the first heavy hole subband (CB1-HH1) are staggered in each of three wells to broaden the gain spectrum. This MQW design is similar in concept to that reported for broad-band LEDs. Gain calculations show a wider and flatter profile than that of a material which consists of three identical quantum wells. The use of non-identical quantum wells allows tailoring of the wavelength range and emphasis on particular bands of the gain spectrum through preferential population of the wells. Our tuning experiments show that this is possible using the feedback of an external cavity grating which induces carrier redistribution to a specific well through mode competition and spectral variations in carrier lifetime in the staggered thickness QW structure.

The strained triple QW laser material was grown at UNM using MOCVD, with 1.5 μm $\text{Al}_{0.70}\text{Ga}_{0.30}\text{As}$ cladding layers and 0.15 μm graded AlGaAs separate confinement layers. The gain region consisted of three $\text{In}_{0.2}\text{Ga}_{0.8}\text{As}$ QW's of 80, 60, and 45 \AA thicknesses, separated by 150 \AA $\text{Al}_{0.25}\text{Ga}_{0.75}\text{As}$ barriers. Ridge waveguide lasers (9 μm wide) were fabricated by standard contact photolithography. After cleaving into 150-300 μm long bars, a two layer anti-reflection (AR) coating of $\text{HfO}_2/\text{MgF}_2$ was electron-beam evaporated onto one facet (witness piece reflectivity was <1.3% with a center wavelength of 950 nm).

Lasers were soldered onto copper heat sinks and mounted onto a thermoelectric cooler. The external cavity consisted of an objective lens (Newport F-L20) that collimated the light from the AR coated side of the laser and directed it onto a 1200 line/mm ruled diffraction grating mounted in a Littrow configuration. Output from the diode was collected with another identical objective

lens, coupled into a multimode fiber, and fed into an optical spectrum analyzer. The AR coating and the short cavity length were necessary to suppress the Fabry-Perot (FP) modes of the cavity to allow the feedback from the grating to determine the lasing wavelength. We obtained optimum tuning results when the wavelength of minimum reflectivity of the AR coating was aligned to the peak in the spontaneous emission. For a 150- μm cavity length laser, good external cavity tuning was achieved with an AR coating of 2% or less at the spontaneous emission peak.

Figure 12 compares the calculated modal gain profile of the staggered thickness well structure with that of a MQW with three identical 80 Å $\text{In}_{0.2}\text{Ga}_{0.8}\text{As}$ wells. Only the $n=1$ levels were included in the calculation. For the same total sheet charge density, the gain of the MQW with staggered QW thicknesses is noticeably wider and less peaked. The material parameters for the $\text{InGaAs/GaAs/AlGaAs}$ QW systems were taken and spectral broadening was taken into account using a Lorentzian lineshape function. Quasi-Fermi levels are assumed constant across the three wells. The well thicknesses of 80, 60, and 45 Å have calculated CB1-HH1 transitions of 970, 944, and 912 nm, respectively. The central wavelength was chosen to allow for easy spectroscopic coverage of the 942 nm absorption line of H_2O . The photoluminescence spectrum of the material shows three distinct peaks, centered at 975, 950, and 930 nm. Therefore, the actual gain spectrum will be shifted and roughly 13 nm narrower than the calculated one.

For a 155- μm semiconductor gain length device which had an AR coating on one mirror and a slightly angled facet on the other, a maximum CW tuning range of 80 nm (from 901 nm to 981 nm) was obtained. The threshold current, I_{th} , was 95 mA at the extreme edges of the tuning range and optical powers were typically several mW. The tuning of the laser to short wavelengths was limited by the onset of parasitic lasing in the internal FP cavity (see Fig. 15(a).) A 70 nm tuning range was achieved with a lower I_{th} of 32.0 mA at the extreme edges of the tuning range in a second 155 μm device with parallel facets; this is less than half of the I_{th} reported by Hall et al. [2] using a stepped-QW laser with a similar cavity length. These results are attributed to the use of an MQW, which yields a lower I_{th} in short cavity lasers, and the staggered thickness wells, which broaden the gain compared to the case of identical wells. A third laser with a 287 μm gain length tuned to longer wavelengths than the first two, bringing the combined tuning range to 86 nm (901-987 nm) for all devices. Figure 13 shows the threshold current as a function of wavelength, and Figure 14 details the variation in output power. The minimum threshold current for the 155- μm laser was 22.1 mA at 938 nm; with the current kept near I_{th} while adjusting the grating, the laser tuned over 60 nm with only a 3 dB change in optical power. The 32 mA maximum I_{th} for the 70 nm tuning is the smallest of which we are aware for this tuning range.

When operating near 980 nm, it was observed that the amplified spontaneous emission (ASE) bulge in the spectrum near 940 nm was less pronounced than when lasing near 910 nm, as shown Figure 15. For lasing at sufficiently long wavelengths, only the lowest energy well can provide gain, and any carriers in the higher energy QW's only contribute to spontaneous emission. Thus, the suppression of ASE near 940 nm while lasing at 980 nm indicates a preferential population of the lowest energy well. When lasing at shorter wavelengths, all three wells contribute to the gain; therefore, all three wells are populated. Without preferential population of one well, there is no mechanism for suppressing the ASE. The preferential population of the lower energy well suggests that the external cavity feedback reduces the carrier lifetime in the lowest well relative

to the others, allowing lasing mode competition to cause a redistribution of the carriers among the wells, draining carriers from the higher energy wells and populating the lowest energy well. This redistribution of carriers would modify the gain profile, increasing the gain of the long wavelength modes. As noted above, at 300 K the MQW system seeks quasi-Fermi levels which are essentially flat across the QW's; yet the present work shows that the flatness of the quasi-Fermi levels can be affected through the carrier redistribution caused by strong feedback.

Summary

A tuning range of 70 nm was obtained from a device at a current of only 32.0 mA. While the CW tuning range was not as large as some previously reported results for the 0.9-1.0 μm range, the threshold current was lower than any of which we are aware. A second device of the same material provided 80 nm of tuning; a total tuning range of 86 nm was observed for the staggered-thickness QW structure. The redistribution of carriers from the spontaneous modes to the lasing mode is currently under investigation. We speculate that this effect is due to a redistribution of carriers between wells resulting from an interaction between the cavity modes and the gain media, an effect which would not be possible in a material composed of three identical wells. The staggered thickness QW material also shows a broader, flatter gain profile than that of a material which consists of three identical QW's; in addition, it allows for the suppression of ASE while lasing at long wavelengths. Future material designs will incorporate wells spaced out further in wavelength to give additional broadening of the modal gain profile.

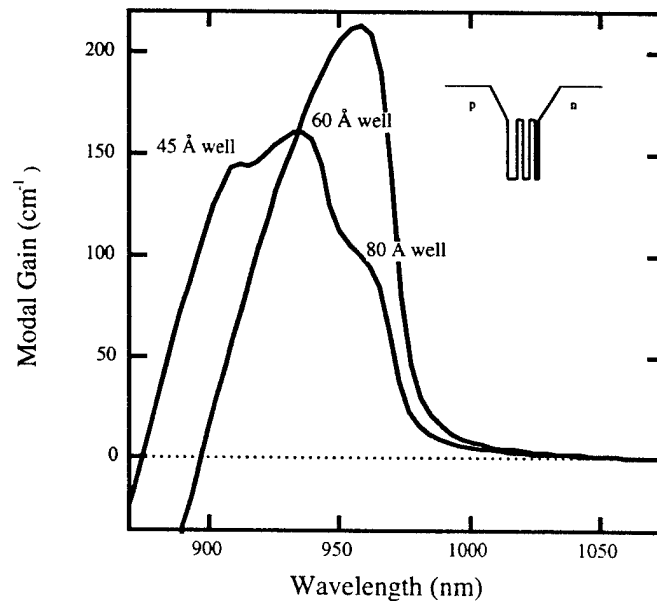


Figure 12. Calculated modal gain profile for staggered thickness quantum well material (solid line) and for three identical 80Å $\text{In}_{0.2}\text{Ga}_{0.8}\text{As}/\text{Al}_{0.25}\text{Ga}_{0.75}\text{As}$ quantum wells (dotted line). A constant quasi-Fermi level is assumed. Sheet density is $1.75 \times 10^{12} / \text{cm}^2$.

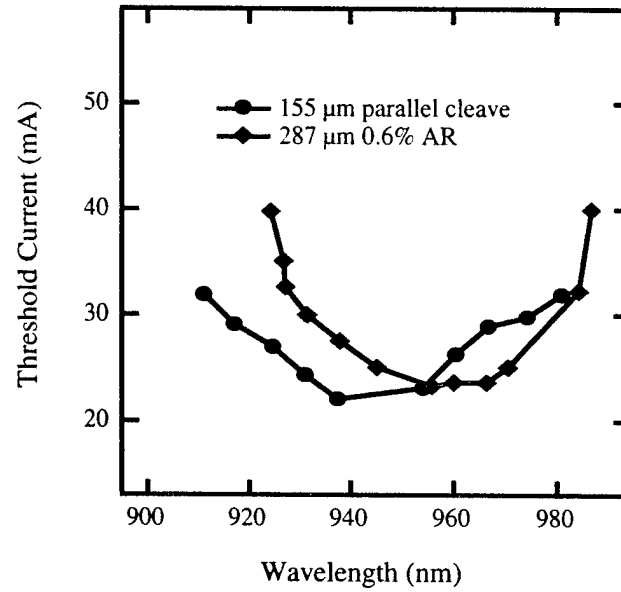


Figure 13. Threshold current as a function of wavelength for two devices with different cavity lengths.

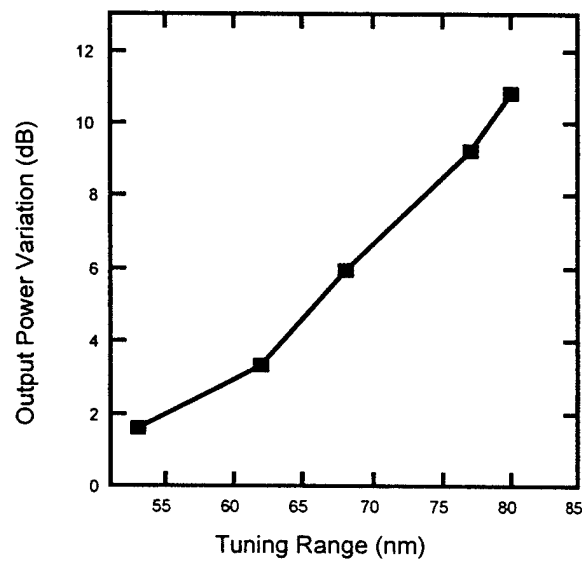


Figure 14. Variation in output optical power as a function of tuning range, with the current kept just above I_{th} . The variation is defined as the highest output power less the lowest output power measured across the tuning range.

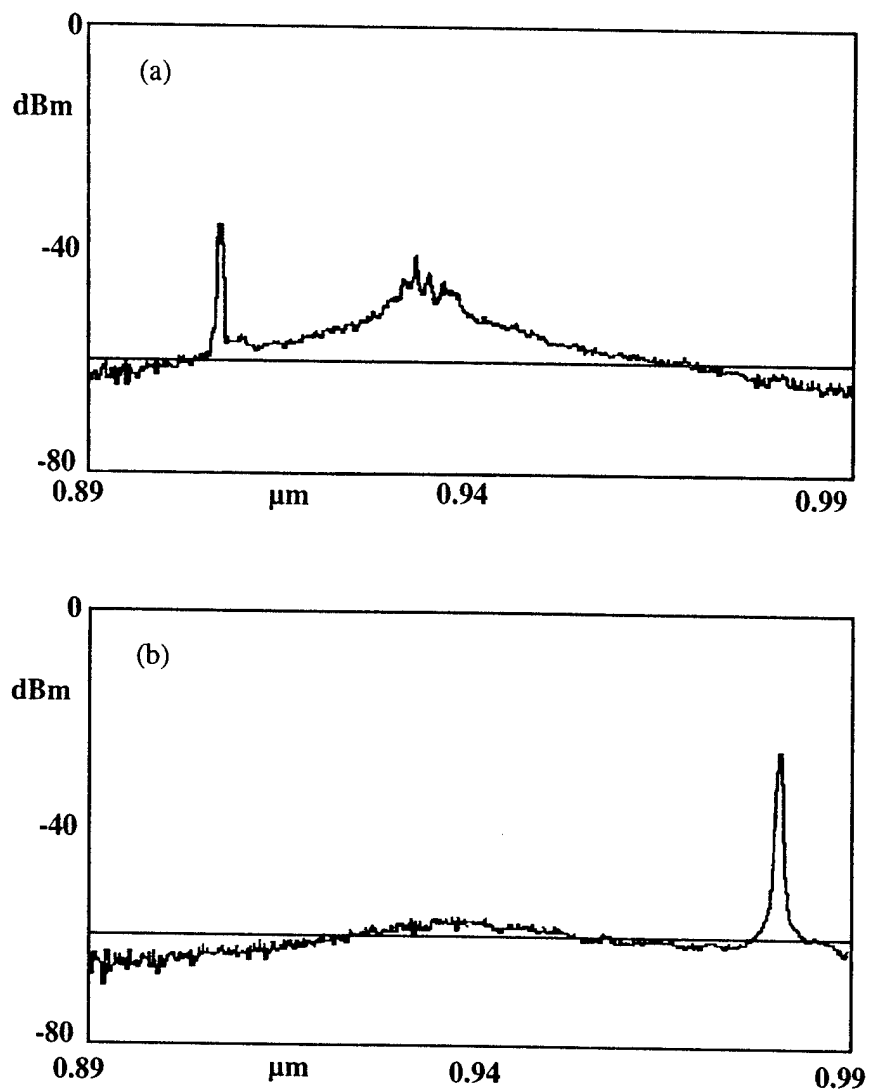


Figure 15. Spectral characteristics of a 155 μm external cavity tuned laser diode. Lasing wavelength for (a) is 911 nm; lasing wavelength for (b) is 981 nm. The current is 32 mA. Note drop in ASE at long wavelengths. The -60 dB line has been added to aid the eye. The lines near 940 nm in (a) are due to residual cavity effects and limit the tuning range at the shorter wavelength; they are not present except when near the short wavelength extreme of the tuning range.

Focus Area: Optical Interconnect Information Networks

Tasks: Free-Space Board Level Interconnects
(520) 621-6172, kostuk@ece.arizona.edu)

Personnel

R. K. Kostuk

S. Kemme

R. Boye

K. F. Zhou

Significant Results

During the past quarter detailed designs for the new version of the low-latency interconnect module were worked out. This version will include a Motorola OPTOBUS VCSEL transmitter array and receiver array as the optoelectronic interface. We received a development board from Motorola with the drivers and amplifiers for the 10 element transmitters and receivers. The sources and receivers will be connected to the module through fiber ribbon arrays with standard MT connectors. This will allow a very versatile arrangement in that the modules can now be cascaded in a fiber optic network which extends the capabilities of optoelectronic components currently under development.

The performance characteristics of VCSELs used in Optobus transceivers from Motorola were measured. These included the beam divergence and wavelength variation of VCSELs within the same array, different arrays within the same module, and for VCSELs in different Optobus modules. This information will be used to design optical elements for the minimum latency interconnect configuration with an array of VCSELs, and for the parallel distribution system.

New holographic gratings were designed for operation at a wavelength of 850 nm which is the nominal wavelength for the Motorola VCSELs. These gratings were formed in photoresist using HeCd and Argon ion lasers. The gratings are designed to divide an incoming array of laser beams into three equal amplitude beams to propagate to the three adjacent faces of the Connection Cube module. We are currently optimizing the exposure and development process. Once this is complete we will etch the resist gratings into the supporting fused silica substrates, and then investigate their transfer into plastic through replication. The replication studies will be done in conjunction with Donnelly Corporation.

A paper is in preparation on the analysis of optical interconnect interface circuitry, and a second paper was submitted on the operating characteristics of VCSELs.

Focus Area: Optical Interconnect Information Networks

Task: Optoelectronic Interconnection Technologies for High Capacity Optical Networks
(505-277-5605, cheng@chtm.eece.unm.edu)

Personnel

J. Cheng (PI)
H. Q. Hou, SNL
M. J. Hafich, SNL
J. C. Zolper, SNL
K. L. Lear, SNL

Significant Results

Computer systems of the future will feature multiple electronic processors linked to form an interactive network with parallel processing capabilities. The objective of this program is to investigate the application of new optoelectronic technologies to interconnect high speed processors using a reconfigurable optical network that provides a large bandwidth and parallelism, as well as increased efficiency and data throughput. Interconnects for such systems must allow the processors to communicate simultaneously with each other and with shared resources on separate modules, while allowing high-speed, dynamic reconfiguration.

Our approach is based on the dynamic reconfiguration of a multi-stage, multi-path, spatial routing network consisting of simple optoelectronic switch arrays that provide parallel optical links between nodes, and electrical access to an associated electronic processor or shared memory module. Optoelectronic integration results in compact switching matrices that allow multiple optical data channels to be spatially routed simultaneously through dynamically reconfigurable paths, thereby achieving a large aggregate bandwidth. Any node in the network can be connected to any other by selecting a path through the closed ring switching fabric through a small number of intermediate hops. To transmit, receive, and re-route optical data, each node possesses an optoelectronic switch that contains an optical source (VCSEL) and a photodetector, and the electronics to convert digital data between electrical and optical input/output formats.

To implement such a network, we have developed an integrable and dynamically reconfigurable optical switching technology with simple optoelectronic interfaces. The switching devices are based on the integration of vertical-cavity surface-emitting lasers (VCSELs) with GaAs heterojunction bipolar transistor (HBT) technology, and with a variety of photodetectors that included p-i-n photodiodes (PINs), heterojunction phototransistors (HPTs), and resonance-enhanced quantum-well detectors (REDs). The integration of these photonic and electronic elements provides functional integration of the photonic switching and optoelectronic conversion capabilities in each switch array. Each switch node can thus receive, transmit, or optically re-route optical data to other nodes in the network. Monolithic switches integrating VCSELs with HPTs have achieved both photonic and optoelectronic switching at a data rate of >200 Mb/s, while those based on PINs and HBTs have achieved switching at data rates of >500 Mb/s. In order to achieve this switching performance, we have developed efficient 850 nm GaAs VCSELs

(with slope and power conversion efficiencies of 45% and 22%, respectively), as well as self-aligned GaAs HBTs with high current gain (>150).

We have also developed integrated binary optical switch arrays that can route either optical or electrical data to other nodes in a dynamically reconfigurable manner. The input ports of each switch consists of two closely spaced, electrically isolated photodetector segments (e.g., PINs or HPTs), each of which forms a separate optoelectronic switch with a different HBT and VCSEL (optical output port). The transmission path can be programmed by electrically selecting each switch, making the routing patterns dynamically reconfigurable. Each switch is connected to a processor, and performs both the photonic switching and optoelectronic conversion functions. Arrays of such nodes form a multi-stage switching network that allows the processors to communicate through parallel optical interconnections. We have made 1×8 arrays of PIN/HBT/VCSEL switches, and achieved routing at a data rate of 500 Mb/s. Multi-stage optical switching operation has also been demonstrated by optically cascading three optical switch arrays, and using optical fibers as the transmission medium. Each switch can achieve a peak differential dc optical gain of 18 and an ac optical gain of four.

The performance of individual switches functioning as optical transceivers has been characterized in fiber transmission experiments. A monolithic PIN/HBT/VCSEL switch is used as the optical source, and another switch is used as the receiver. The optical input and output are butt-coupled to an optical fiber with a length that varies from 0.5 m to 1 km. Optical data was transmitted across a 1 km length of multi-mode fiber at a data rate of 650 Mb/s, and a bit-error-rate of $\sim 10^{-9}$ was achieved at a signal level of -12 dBm.

To improve the speed and responsivity of the optoelectronic switches, we have developed an improved self-aligned HBT process that uses an InGaP emitter and an air-bridge design, as well as a novel photodetector design that uses a vertical-cavity resonance-enhanced quantum-well photodetector (REPD). Our goal is to extend optical switching operation beyond 1 Gb/s. To facilitate the monolithic integration of all the photonic elements (source and detector arrays) on a single chip, we developed a novel epilayer design in which the REPD cavity is embedded within the cavity of the VCSEL, allowing the two to be integrated in a manner that does not compromise the performance of either device. The REPD cavity is realized by chemically removing some of the AlAs/AlGaAs quarter-wave layers in the upper DBR mirror. Wavelength-matching source and detector arrays have been made at both the 980 nm and 850 nm wavelength bands. The 980 nm REPD structures achieved resonant photodetection with a peak quantum efficiency of $\sim 87\%$, compared to a theoretical efficiency of $>95\%$, with a spectral width of 2 nm. The VCSELs demonstrated very good cw operating characteristics, with a low threshold current (1.5 mA to 2.5 mA) for devices with an active area diameter varying from 8 μm to 16 μm , a low threshold current density (850 A/cm²), and a differential quantum efficiency of 55 percent.

A new format for implementing the reconfigurable optoelectronic switch array has been created, in which all the photonic components (VCSEL and REPD arrays) and electronic components (HBT circuits) are individually optimized and separately integrated on different wafers.

Focus Area: Optoelectronic Information Networks

Task: Interface Electronics from WDM optical interconnects to the DASH Multiprocessor Machine
(415-723-9775, harris@snowmass.stanford.edu)

Personnel

J. S. Harris
C. J. Chang-Hasnain
J. W. Goodman
J. Lam
W. Martin

Significant Results

A new design is being developed for the WDM system. The Dragone can be used to define the channels in the WDM system. With a small addition to the Dragone layout the output power at each wavelength can be measured. This measurement can be feedback to effect wavelength control of a tunable laser. The feedback system has been modeled and designed. We are now in the process of buying the needed electronics and setting up the required optical system.

A diagram of the feed back system is shown in Figure 16.

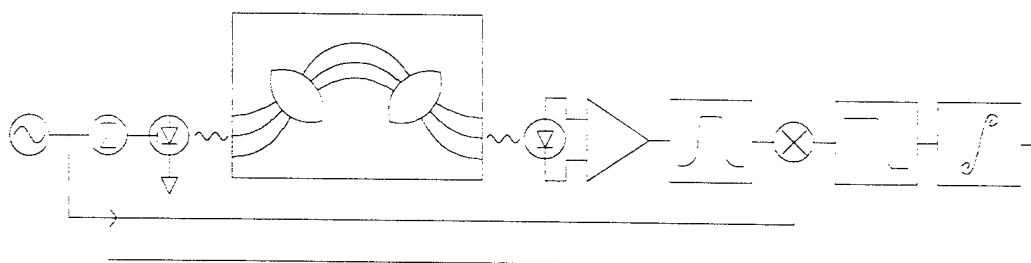


Figure 16. Feedback system modeled and designed.

The VCSEL in this design is the electronically tunable micromachined microcavity VCSEL developed by fellow Harris students, Michael Larson and Fred Sugihwo. The system is a frequency locked loop that has been adapted for optical devices. The feedback loop consists of the modified Dragone, a sine wave oscillator, a VCO (the tunable VCSEL), a photodiode, an analog multiplier, a low pass filter, and a bias circuit. The tuning voltage of the laser is set by the bias circuit. The output of the sine wave oscillator is added to the tuning bias voltage. The resulting laser tuning voltage has a small amplitude AC signal on top of a DC bias. The AC signal causes the frequency of the laser to vary with time. The output of the laser is bandpass filtered in the wavelength domain by the modified Dragone. The photodiode converts the output power into voltage. That voltage is then multiplied with the oscillator output and low pass filtered. The resulting signal is then feedback to adjust the DC bias in order to maintain wavelength stability.

With wavelength stabilization a WDM system can be used as a parallel clockable datalink for speed distance products up to 1 GHz and 1 Km. This will improve latency significantly in the optical interconnect for the FLASH multiprocessor because the parallel to serial and serial to parallel conversions are no longer needed.

A system which has controllable tuning of laser wavelength would allow for many interesting types of networks to be built. In addition to the multichannel per node system like the FLASH multiprocessor interconnect being developed in this project, a distribution network where one node transmits on many channels and receiver nodes tune to the channel(s) they need, or a one link per WDM channel between multiple machines on the same fiber network can be easily built.

A version of the Dragone has been fabricated by PIRI. It has been tested. The results are good with low loss, $< 5\text{dB}$, and small channel to channel variation $< 3\text{ dB}$. A new version of the modified Dragone is currently being designed at Stanford.

Focus Area: Optoelectronic Information Networks**Task: Fabry-Perot MQW Spatial Light Modulators
(415) 723-9775, Harris@Snowmass.Stanford.edu)****Personnel**

J. S. Harris

J. S. Powell

J. A. Trezza

Significant Results

To perform extremely efficient optical switching, routing, and logic, photonic switches and gates should ideally be conservative (preserving optical input power) and reversible (inputs and outputs can be interchanged). Such a device forms a natural and complete primitive for decomposing logic functions. The transmission reflection modulators we have developed (known as X-modulators) when used as an X-gate (inputs on both sides of the device), or as a single device controllable exchange function—an exchange bypass switch). Its current implementation is electro-optical, with one electrical control and two optical data inputs. It is the logical implementation of a Fredkin gate (3-input, 3-output conservative, reversible gate). Logic that is conservative and reversible can have very low power dissipation, in that it conserves the number of 1's in the input and output. The reversibility of the gate increases its architectural functionality. There exist only two distinct 3-input 3-output conservative invertible functions (using a counting argument). One of these functions is associated with the "Fredkin" gate, the second function has an obvious rotational symmetry, an "output symmetric function"—as opposed to classical (input) symmetric functions (e.g. AND, OR, Exclusive-OR). Because of this symmetry, we refer to this function as R-(right rotation) or L- (left rotation) functions, modulators, or gates. It turns out that R-gates are essentially associated with routing type function, because they perform the role of an "optical circulator".

X-gates and R-gates are both logically complete since both gates can be represented as two or three multiplexers, the basis of the Shannon expansion of Boolean functions. A very natural configuration of the X-gate directly implements the exclusive-or function, needed by most data security and error correcting code algorithms. X- and R-gates as devices are very versatile and thus promising for use in photonic switching, routing, communication, and computation.

We demonstrated an X-modulator based on the quantum well Fabry-Perot modulator techniques we have investigated extensively over the last 8 years. The device consists of a cavity in which two optical beams are incident upon the structure as shown in Figure 17. The first impinges from the top of the device, the second from the bottom. In one state of operation, the device is highly reflective and the beams are output to their original side of the device. In the other state the device is transmissive and the beams cross and pass through the structure, thus performing an exchange operation. After discussing the basic device structure, we present several systems applications of the device (complex logic functions and optical switching and routing) and finally some refinements to the device to make it more amenable to systems applications.

As previously stated, X- and R-gates are useful for computation, coding, switching, and routing. To begin with, we have demonstrated the logic and routing functionality of the X-gate by stacking two of the devices in series and verifying the expected output functions. Because large optical output is available in both states, an incident optical signal at A or B could be routed to any of the three optical outputs, depending on the state of the electrical inputs, D and E. A single X-gate with an electrical control signal performs a simple 2x2 exchange operation. This operation is useful for sorting and routing networks. Using regular arrays of these devices, we can easily construct a 4x4 (or in general, an NxN) optical crossbar switch, permuting the four optical inputs to the four optical outputs in a conservative manner (number of 1's is preserved).

So far we have looked at applications of X-gates for building optical routing and switching architectures. A single R-gate can be constructed from 2 X-gates in cascade, by having each X-gate exchange 2 different inputs. By studying the Boolean functions of the R-gate, it is clear that the R-gate may be realized using three 2-way switches; therefore, less than the four 2-way switches are needed if two X-gates are used. This indicates that it is more efficient to have both types of gates available. We also note that this implementation requires optically controlled X-gates or at least optoelectronic conversion for the control signals. This fact also indicates that the R-gate is a natural 'all-optical' device (control and data signals are optical). An R-gate type router can be obtained by a non-minimal but symmetric arrangement of 3 X-gates.

As previously mentioned, our test devices as originally designed have a maximum transmission of 60% and a minimum transmission of about 6%, hence a contrast ratio of 10. Ideally these percentages should more closely approach 100% and 0%, or possibly even greater than 100% in the maximum transmission case (i.e. amplification) for fan-out purposes. We are attempting to overcome this problem by investigating structures that include two layers, or zones; one that performs the modulation of the light (X-modulator, for example) and one that will amplify the light, in essence restoring the energy that is lost in the modulator. This work is still in progress and experimental results are expected by the conference date.

As an initial design for such a device, we consider two possible configurations. In the first configuration, the gain quantum wells are contained within the same Fabry-Perot cavity as the absorptive wells. In this structure there are two individually biased regions, so that we end up with a n-i-p-i-n stacking of layers. The gain layers are forward biased to provide a gain of approximately 600 cm^{-1} per well, and the absorptive wells are switched between around 11,000 and 50 cm^{-1} per well loss using the quantum confined Stark effect. It may also be desirable to switch the gain layers between gain and loss, however the speed of this switching is limited by the amount of time required to sweep the carriers out of the quantum well region. We have simulated the device in the case that only the absorptive wells are switched. The results of this simulation are shown in Figure 18. As can be seen in the figure in one state, the device is highly reflective (95% reflection, ~0.3% transmission). Other structures may produce a higher reflectivity than 95%, but are more difficult to correctly grow using MBE. In the transmissive state, the device amplifies the signal transmitted by a factor of ~2 (with ~5% reflection). Thus, we have demonstrated that our devices can incorporate gain layers within the optical cavity to restore some of the light lost to absorption. The optimal reflection and transmission percentages

depends upon the architectural configuration of the devices involved. In some cases an asymmetric device such as this may be an acceptable solution.

A second possible device structure would consist of two cavities, where the coupling between the modulator cavity and the gain cavity is small to prevent coupled cavity effects. In this case, a large reflectivity mirror is required between the two cavities, which results in a high Q modulator and makes our design difficult to realize. A better solution may involve anti-reflection coating the top of the device so that there is essentially only one cavity present. In this case, the gain layers are only single or double pass depending on the state of the device and thus a larger number of wells would be required. We feel that the first configuration is the more promising of the two, however both designs are under investigation.

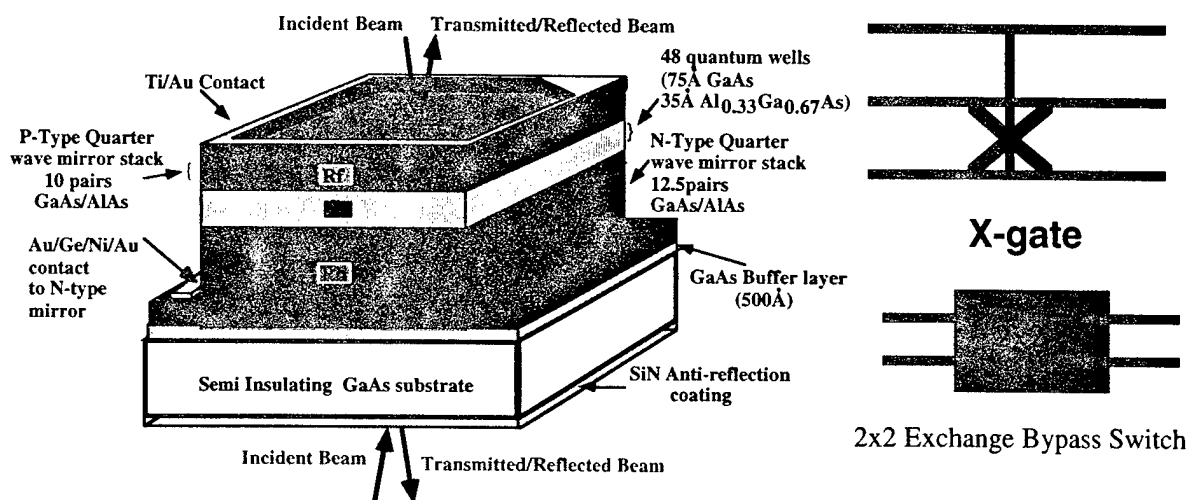


Figure 17: Schematics of a vertical cavity X-modulator

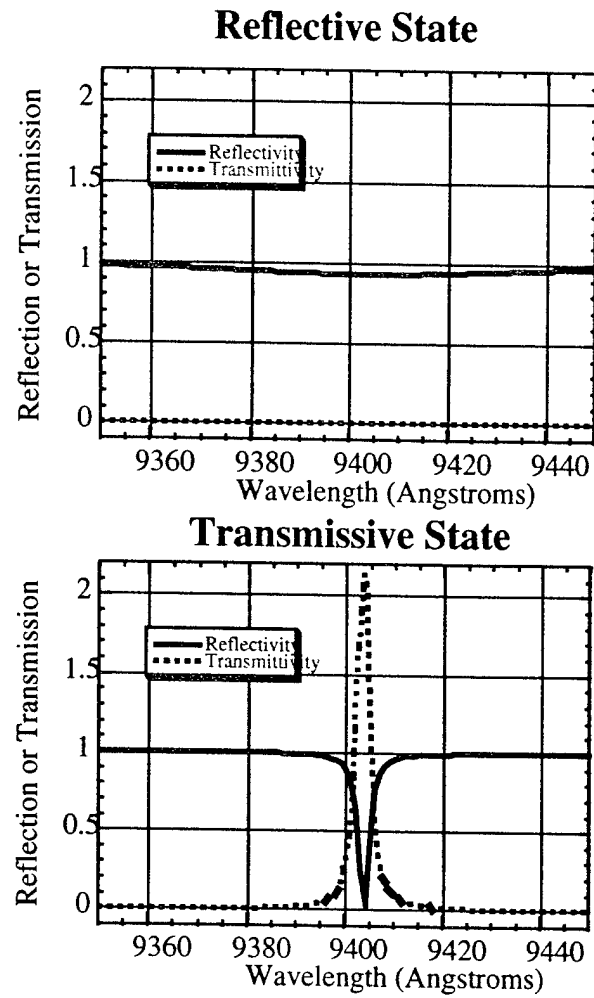


Figure 18: Simulation of reflection/transmission modulator with gain

Focus Area: Optoelectronic Interconnection Networks**Task: Ultrafast All-Optical Modulator**

(520-6214649; peygba@ccit.arizona.edu)

Personnel

N. Peyghambarian (PI)

D. Mathine

S. Ten

Significant Results

Emerging all-optical communication technologies require nonlinear optical materials with ultrafast response times. Semiconductor multiple quantum wells (MQWs) have attracted significant attention because of their large excitonic room temperature nonlinearity. However, the nanosecond recovery times of MQW nonlinearity controlled by carrier lifetime has been an obstacle for high speed device applications. To overcome slow recovery times in MQWs several approaches have been explored: fast absorption recovery in tunnel structures, defects generation by doping or proton implantation, low temperature growth (LTG) of semiconductor materials.

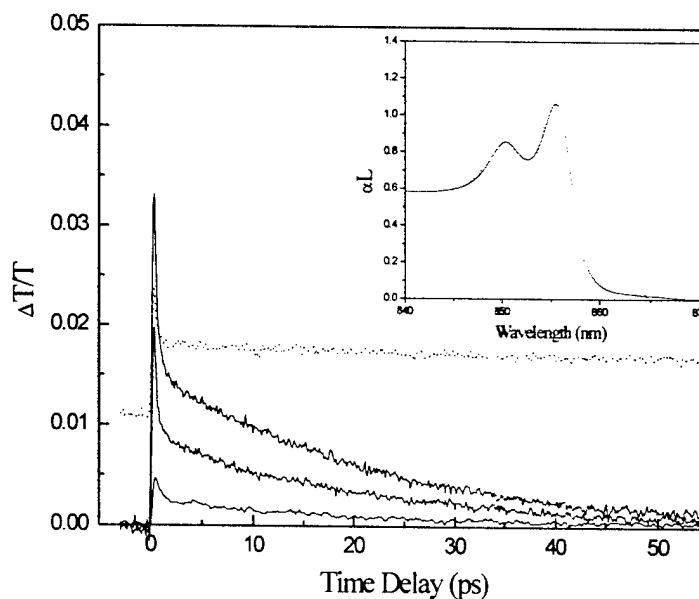


Figure 19. Time resolved differential transmission data recorded for neutron irradiated (fluence of $1.96 \times 10^{16} \text{ cm}^{-2}$) 120 Å GaAs/(Ga_{0.7}Al_{0.3})As MQW (solid lines) at carrier densities of 1.7×10^{11} , 10^{11} and $3.3 \times 10^{10} \text{ cm}^{-2}$ and the same non-irradiated sample (dotted line) at carrier density of $3.3 \times 10^{10} \text{ cm}^{-2}$. The inset shows linear absorption spectra of neutron irradiated (solid line) and non-irradiated (dotted line) MQW.

We have demonstrated that sharp excitonic features and ultrafast carrier lifetimes can be achieved in neutron irradiated (Ga,Al)As/GaAs. Neutron irradiation generates defects which act as very efficient recombination centers without excessive broadening of the exciton absorption resonance. We investigated a (Ga,Al)As/GaAs MQW sample which was conventionally grown (substrate temperature 630 C) by molecular beam epitaxy. It consisted of 50 periods of 120 Å GaAs wells separated by 100 Å (Ga_{0.7}Al_{0.3})As barriers. Sharp excitonic features could be

observed in absorption spectrum at room temperature (see inset in Figure 19). Irradiation by fast neutrons was performed in the University of Arizona nuclear reactor with 1 MeV equivalent GaAs fluence of $1.96 \times 10^{16} \text{ cm}^{-2}$.

Linear absorption spectra of the MQW sample before and after irradiation are shown in the inset in Figure 19. Sharp excitonic features dominate both spectra with the neutron irradiated sample showing a slight broadening of the light and heavy hole exciton absorption resonances, reducing the maximum absorption by 12%. Time-resolved heavy hole exciton absorption recovery of the neutron irradiated MQW sample is depicted in Figure 19 for different densities of photoexcited carriers. Two components can be seen in these data. The first is due to the dynamic Stark effect and second, slower component, is controlled by the recombination of real carriers. An exponential fit of the second component a time constant of 21 ps. The lifetime of the photoexcited carriers in our sample before irradiation was longer than the period between optical pulses (12.5 ns) and this resulted in From the non-recovered absorption changes in the differential transmission pump/probe data (see dotted curve in Figure 19). Thus, we demonstrated a three order of magnitude reduction of the carrier lifetime in our MQW sample with only small changes in the excitonic absorption features.

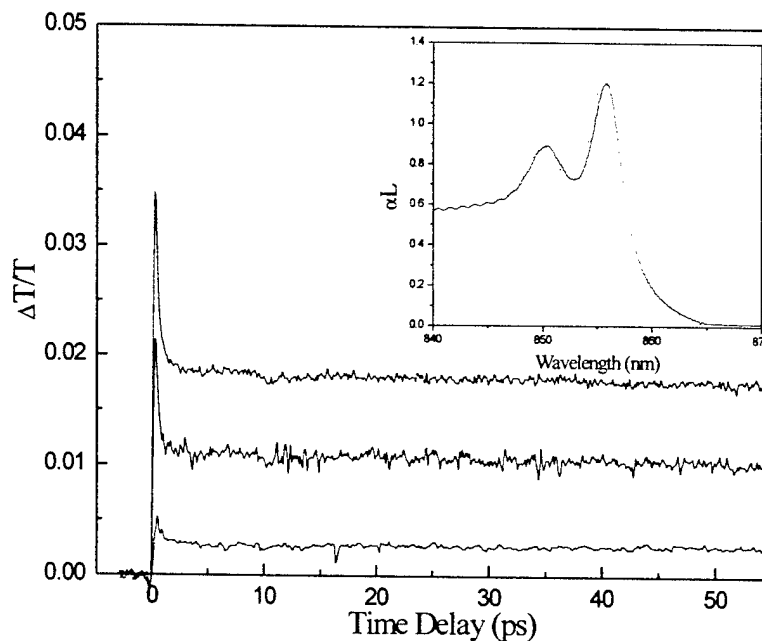


Figure 20. Time resolved differential transmission data recorded for γ -irradiated (fluence of $1.24 \times 10^8 \text{ Rad}$) 120 Å GaAs/(Ga_{0.7}Al_{0.3})As MQW at carrier densities of 1.7×10^{11} , 10^{11} and $3.3 \times 10^{10} \text{ cm}^{-2}$. The inset shows linear absorption spectra of γ -irradiated (solid line) and non-irradiated (dotted line) MQW.

Neutron irradiation in a nuclear reactor is always accompanied by a certain dose of γ -rays. We estimated the total fluence of γ -rays in neutron irradiation to be approximately 10^8 Rad . γ -rays are also known to reduce carrier lifetime. To elucidate the contribution of γ -irradiation we irradiated our MQW sample with γ -rays from Co⁶⁰ source. The total fluence was $1.24 \times 10^8 \text{ Rad}$ - slightly higher than for neutron irradiation. The results are depicted in Figure 20. First, we can see that γ -irradiation does not affect the linear absorption spectrum of our sample (see inset in

Figure 20). Second, it obviously reduces carrier lifetime since differential transmission recovers completely by the beginning of next optical pulse in contrast to the non-irradiated sample (dotted curve in Figure 19). However, the absorption recovery time is too long to be observed on the 50 ps time scale. We therefore, arrive at the conclusion that the radiation damage resulting in the dramatic reduction of carrier lifetime comes primarily from the neutron irradiation.

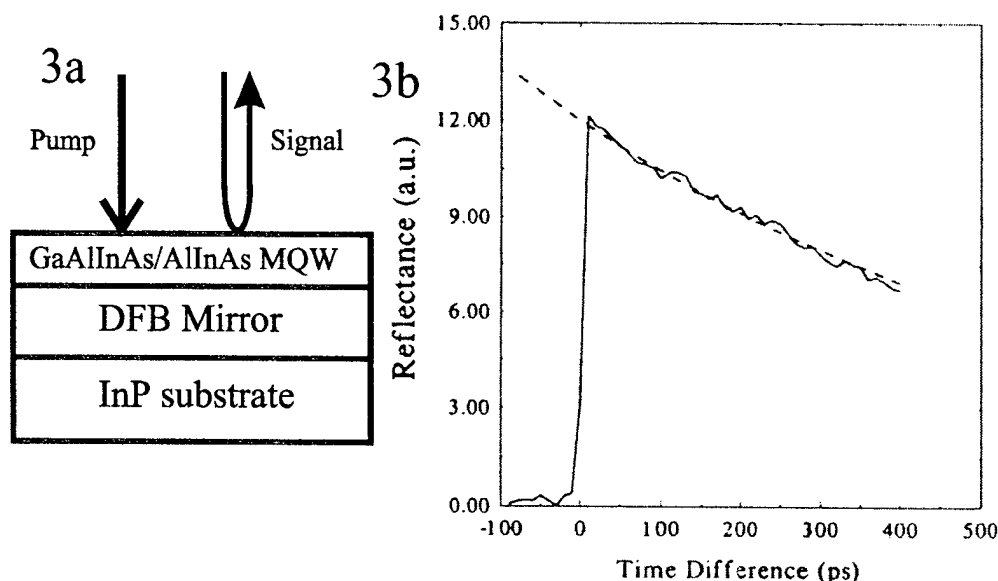


Figure 21. (a) The schematic diagram of the MQW all-optical asymmetric reflection modulator (b) the recovery of the reflectivity of the modulator before neutron irradiation.

We utilize the reduction of carrier lifetime by neutron irradiation in an all-optical modulator for the 1.3 μm communication wavelength. For this purpose a high contrast GaAlInAs MQW asymmetric reflection modulator has been designed and fabricated (see Figure 21a). It consists of a 65 period 69 \AA $\text{Ga}_{0.376}\text{Al}_{0.094}\text{In}_{0.53}\text{As}$ well/89 \AA $\text{Al}_{0.48}\text{In}_{0.52}\text{As}$ barrier MQW spacer on top of a 24 period 936 \AA $\text{Ga}_{0.3}\text{Al}_{0.18}\text{In}_{0.52}\text{As}$ /1003 \AA $\text{Al}_{0.48}\text{In}_{0.52}\text{As}$ quarter-wave stack back mirror. This structure was grown lattice matched on a InP substrate by MBE. The Fabry-Perot cavity which enhances the MQW nonlinearity is formed by the air/spacer interface ($R_f=0.31$) and the quarter-wave stack back mirror ($R_b=0.92$). This modulator exhibit more than 30 dB on/off contrast ratio at the wavelength of 1314 nm. The recovery dynamics of the modulator was measured in a time-resolved pump/probe geometry (see Figure 21b). The reflectivity of the modulator recovers exponentially with the time constant of 725 ps. The recovery time is controlled by the carrier lifetime typical for the MQW material. We neutron irradiated three different pieces of the same modulator with fluences of 10^{16} cm^{-2} , $2 \times 10^{16} \text{ cm}^{-2}$ and $4 \times 10^{16} \text{ cm}^{-2}$. If the carrier lifetime reduction occurs with the same rate as in GaAs MQWs we expect to fabricate a high-contrast modulator with 10 ps recovery time.

Focus Area: Optoelectronic Information Networks

Task: Enhanced-I Si MSM Detectors
(505-2777-6433. brueck@chtm.eece.unm.edu)

Personnel

S. R. J. Brueck (PI)

K. A. M. Scott

D. R. Myers (SNL)

J. C. Zolper (SNL)

Significant Results

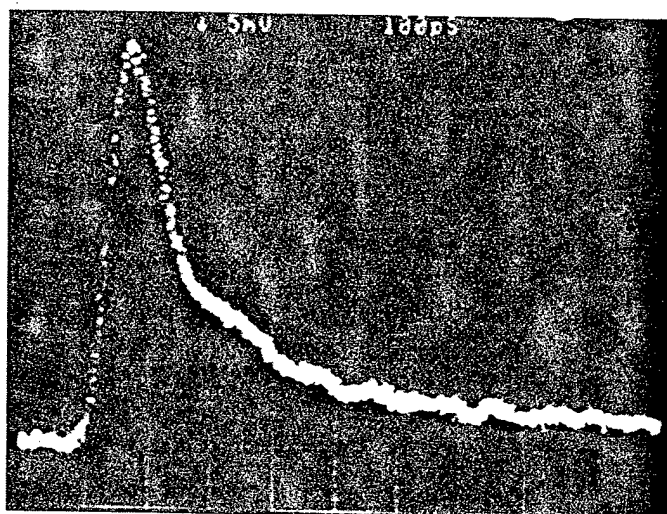
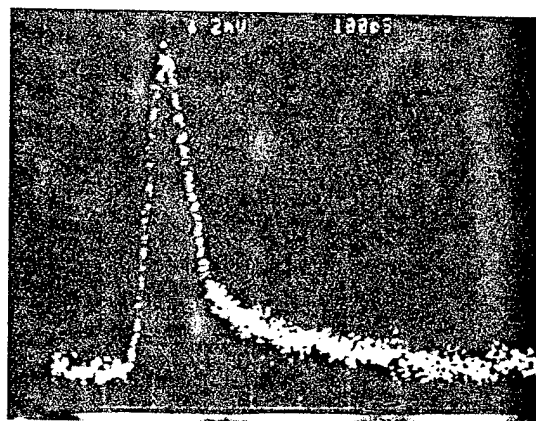
Our task has been to fabricate and study high-speed, CMOS-compatible photodetectors made using bulk Si for near-IR communications wavelengths (~ 760 - 980 nm). The main challenge was to overcome the long absorption length (~ 5 - 20 μm) inherent in silicon at these wavelengths which result in an unacceptable diffusion tail in the impulse response of the photodetectors for high-speed applications. Our solution was to create a damaged layer ~ 1 μm below the Si surface by a simple ion-implantation step to reduce the diffusion tail while maintaining the high-mobility, crystalline region above for carrier transport and making the Ni Schottky contacts. We have studied two types of implantations, fluorine with no annealing and helium with annealing, both of which increase the speed of the devices compared to the unimplanted controls. After the material is prepared, Ni Schottky contacts are fabricated, along with an unimplanted sample as a control, with 10 pairs of interdigitated fingers 3 μm wide with 5 μm spacing. These were then tested for DC responsivity, speed, and frequency bandwidth from 760-980 nm.

The samples were prepared in the following way. Implantation with F ions at 280 keV created a damaged layer consisting of divacancies ~ 0.5 μm below the Si surface. The divacancies remain stable until around 150 C, where they begin to anneal. In the case of He, implantation at 300 keV created a damaged layer 1.4 μm below the surface. When annealed at 900 C for 1 hour, the He permeated out to the surface and the vacancies coalesced to form larger voids approximately 10 nm in diameter, called nanovoids. Also during annealing, the region above the damaged layer is restored to near crystallinity, which improves the mobility of carriers near the metal contacts. The nanovoids are stable up to the annealing temperature. The absorptivity measured for both types of implanted Si ($\sim 10^3$ cm^{-1}) is several orders of magnitude larger than crystalline Si for incident light longer than 750 nm. Thus the divacancy/void layer is a region of enhanced absorption in this wavelength range.

The photodetectors were initially characterized by their DC responsivity. IV curves showed stable back-to-back Schottky contacts for all samples, with both the F- and He-implanted devices exhibiting a lower breakdown voltage (12V vs. 25V for unimplanted) but this was still above the 10V needed for the high-speed characterization. The He- and F-implanted detectors had approximately four times less and ten times less photocurrent compared to unimplanted detectors, respectively. The implantation process left some residual surface damage which accounts for the lower breakdown voltage and traps in the damage layer could explain the reduction in DC photocurrent.

The impulse response to a 150-fs optical pulse from a Ti:Al₂O₃ laser was measured from 760-980 nm. Over the entire wavelength range tested, the implanted detectors were consistently faster than the unimplanted controls, with the F-implanted devices being slightly faster than the He-implanted. Figure 22 shows results at 930 nm for the He-implanted device and the unimplanted control. There is a dramatic reduction in the diffusion tail for the implanted device with approximately half of the peak photocurrent of the unimplanted device. While the F-implanted detectors were faster overall, the device signal had to be amplified to be measured. At 980 nm the FWHM of the impulse response was 80 ps for the F-implanted detector, compared to ~ 120 ps for an unimplanted detector. The limit of the sampling scope used was 75 ps. Data was also taken in the frequency domain and then Fourier transformed show a FWHM of ~ 20 ps for He-implanted and 29 ps for unimplanted. While the numbers are different between the time and frequency domains, the relative increase in speed is still about one-third.

In conclusion, the He-implanted detectors offer a good compromise between increase in speed and loss in peak signal. An additional advantage of the He-implanted detectors over the F-implanted ones is that the He-implanted nanovoid layer, formed by a high-temperature anneal, is temperature hardy up to 900 C.



(a)

(b)

Figure 22. Impulse response of detectors with 5 micron interdigitated fingers at 930 nm made on (a) unimplanted control wafer and (b) He-implanted nanovoid wafer. While a loss in peak signal height is measured in the implanted detector, there is an improvement in the FWHM (100 ps vs. 120 ps) and a dramatic reduction in the diffusion tail.

Focus Area: Optoelectronic Information Networks

Task: Multiple-wavelength vertical cavity surface emitting laser (VCSEL) for WDM inter-processor optical interconnects
(510-642-4315; email:cch@eecs.berkeley.edu)

Personnel

C. J. Chang-Hasnain

G. Giaretta

W. Yuen

Significant Results

Vertical-cavity surface-emitting lasers (VCSELs) are promising for optical fiber communications and interconnects. The surface-normal topology of VCSELs facilitates the integration of devices as one- or two-dimensional arrays. This feature, combined with the inherent single Fabry-Perot mode operation, makes VCSEL one of the most attractive laser structures for wavelength division multiplexing (WDM) applications. In addition, multiple-wavelength (MW) VCSEL arrays with wide channel spacings ($\sim 10\text{nm}$), also known as sparse WDM, provide an inexpensive solution to increasing the capacity of local area networks without using active wavelength controls.

Our effort under this research program has two parts: the fabrication of MW VCSEL array, and the laser design and delivery for WDM optical interconnects. On the first part, we have successfully demonstrated a novel method to epitaxially grow and fabricate MW VCSEL arrays with repeatable wavelengths. On the second part, we have delivered MW VCSEL arrays to Hewlett Packard Laboratory for a sparse multi-mode WDM interconnects system experiments. Both parts of our studies resulted in journal publications and conference presentations. This report is organized as follows. In section I, we will briefly discuss the MW VCSEL work and section II, the new laser fabrication technique we invented for WDM interconnects and some preliminary systems results obtained through collaboration with HPL on WDM interconnects.

(I) Multi-Wavelength VCSEL Arrays**I. 1 Introduction**

Our work on multiple-wavelength (MW) arrays has made major advances. We fabricated MW VCSELs using a patterned-substrate growth technique in conjunction with a location-resolvable in-situ laser reflectometry in a molecular beam epitaxy (MBE) system. A backside pattern is used on the substrate to induce a temperature profile on the growth surface, which in turn determines the growth rate to create MW-VCSELs. We achieved a record wavelength span of 62.7nm , and high repeatability and accuracy of 0.28% . This is the best reported for monolithic laser arrays. There have been several efforts of making multiple-wavelength VCSEL arrays where different methods of varying effective cavity thickness have been explored. Among all approaches, patterned-substrate MBE growth appears the most promising because only one growth is required and accurate wavelength spans can be achieved through in-situ monitoring.

I.2 Basic Technique for Fabrication MW VCSELs

The principle of the patterned-substrate growth technique is based on the dependence of Ga desorption rate (and therefore the GaAs growth rate) on the surface temperature in an MBE system. An intentionally created substrate surface temperature profile can be translated into a GaAs layer thickness profile and thereby the desired lasing wavelength distribution through the equivalent cavity thickness variation.

To utilize the dependence of GaAs growth rate on the surface temperature to produce thickness variations, significant surface temperature difference has to be created by using different thermal contacts in different regions of a single wafer. Also since the surface temperature distribution uniquely determines the lasing wavelength distribution, the thermal contacts have to be uniform across the wafer to produce repeatable VCSEL arrays. Here, we use the approach of directly mounting a backside-patterned wafer onto a molybdenum holder (molyblock) with indium to obtain thermal contacts, as shown in Figure 23. The portion that has indium contact with the molyblock will have a higher surface temperature than other portions of the wafer. The measured temperature difference can be as much as 50 C, more than sufficient to create a large GaAs growth rate difference.

The location-resolvable laser reflectometry is implemented by directing the collimated output beam of a diode laser onto different regions of a patterned substrate where control of the wavelength span is desirable. Due to the interference effect from the layers underneath, growth rates of different regions and the surface thickness changes can be accurately monitored and then determined. Since the laser beam can be focused down to a spotsize as small as 1mm^2 , high spatial resolution can be obtained.

I.3 Experimental Results

Figure 24 shows the measured lasing wavelength under pulsed operation as a function of position in the direction perpendicular to the stripe of the substrate pattern with designed wavelengths marked. The pre-growth optical in-situ measurements show that there is ~15% of Ga desorption rate in the hot region and no desorption in the cold region. The calculated lasing wavelengths in the hot region and cold region based on this information are approximately 941nm and 966.7nm, respectively, whereas the measured wavelengths are 941nm and 964nm, respectively. The lasing wavelength matches exactly in the hot region and presents only 0.28% of deviation in the cold region.

With another heteroepitaxial design incorporating thickness region of graded layers, we achieved VCSEL wavelength span of 62.7nm. This is the largest span achieved for a multiple-wavelength laser array to date, to the best of our knowledge. The CW threshold current for these lasers exhibits fairly weak dependence on wavelength and is essentially flat within 30nm range with the minimum of 1.18mA. The average and standard deviation are 2.16mA and 0.81mA, respectively. Typical optical output level of ~0.8mW is obtained.

I.4 Conclusion

In this program, we demonstrated a patterned-substrate growth technique in an MBE system for making uniform and widely spanned multiple-wavelength VCSEL arrays, and explored the key

aspects involved in implementing this technique. We also developed a location-resolvable optical in-situ calibration method with which the growth rates on different regions of the same wafer can be accurately measured. We demonstrated reproducible multiple-wavelength VCSEL arrays with a record wavelength span, excellent CW lasing operation, sharp and uniform wavelength dispersion, and accurate and repeatable lasing wavelengths. With these desirable characteristics, the devices fabricated by using the techniques described in this paper should be very useful for making multiple-wavelength VCSEL arrays for cost-effective WDM applications.

(II) WDM Interconnects

Highly multimoded MW VCSEL array with 10 nm wavelength spacing was fabricated, characterized and delivered to Hewlett Packard Laboratories for sparse WDM interconnects experiment. Since there are specific wavelength and physical spacing requirements, repeatable arrays with wire bond pads suitable for packaging must be fabricated. Such requirements presented difficulties in our routine fabrication methods and lead us to significant alteration on our design and processing. Eventually we invented a novel processing technique for addressable array and excellent WDM bit-error-rate measurements were obtained.

II.1 Novel Addressable Array Fabrication Method

Independent addressable VCSEL arrays had been reported before for proton implanted VCSELs, whose planar substrate facilitate easy fabrication. With the advances in oxide-confined (OC) VCSELs, showing dramatic improvements in threshold currents and wall plug efficiency, they seem ideal for array applications. However, the oxide confined VCSEL has a nonplanar structure which makes fabricating the electrical interconnects difficult. We introduce a novel and extremely simple two-mask process that uses a single oxidation layer to define the laser aperture and to isolate the interconnects.

Figure 25 shows a typical VCSEL structure with a single AlAs layer, used simultaneously to define the oxide aperture and to isolate the electrical interconnects. Figure 26 shows the two-mask fabrication process. The first step is the deposition and lift-off of the top Ti/Au contacts. Next, an array of VCSEL posts connected by the interconnects to the contact pads are etched just below the active layer. The single AlAs layer is then oxidized. The oxidation process is stopped when the pads and the interconnects are completely oxidized and the laser aperture has reached a desired aperture size. This is accomplished by making the VCSEL posts having a larger diameter than the width or length of the contact pads. This process completely eliminated the need of planarization of OC VCSELs with polyimide or other materials, which all require significant curing time at elevated temperatures that can adversely degrade OC VCSELs.

II.2 Results

The bit error rate measurements of a MW VCSEL fabricated with $\sim 300\mu\text{m}$ long oxide interconnects is shown in Figure 27. The laser was modulated at 622Mbit/sec with a Pseudo Random Bit Sequence $2^{23}-1$. The BER shows no error rate floor and a BER of 10^{-9} was achieved. Furthermore, an open eye diagram was measured at 1Gbit/sec.

In summary we have demonstrated a novel very simple 2-mask process to fabricate very uniform independently addressable VCSEL arrays that combines the simplicity of fabrication of proton

implanted VCSELs with the low threshold, high wall plug efficiency and uniformity of oxide confined VCSEL arrays. The MW VCSEL array delivered to HP operated at 1Gb/s with an open eye and exhibits no BER floor, indicating excellent suitability of WDM interconnects applications.

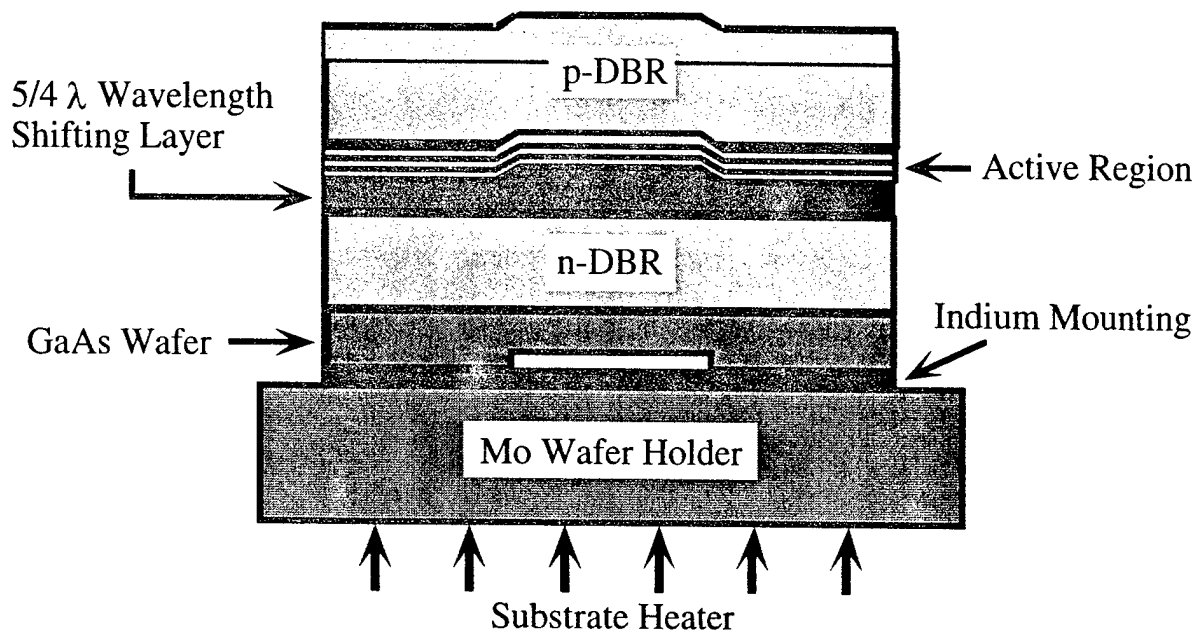


Figure 23. Schematic of the patterned-substrate growth

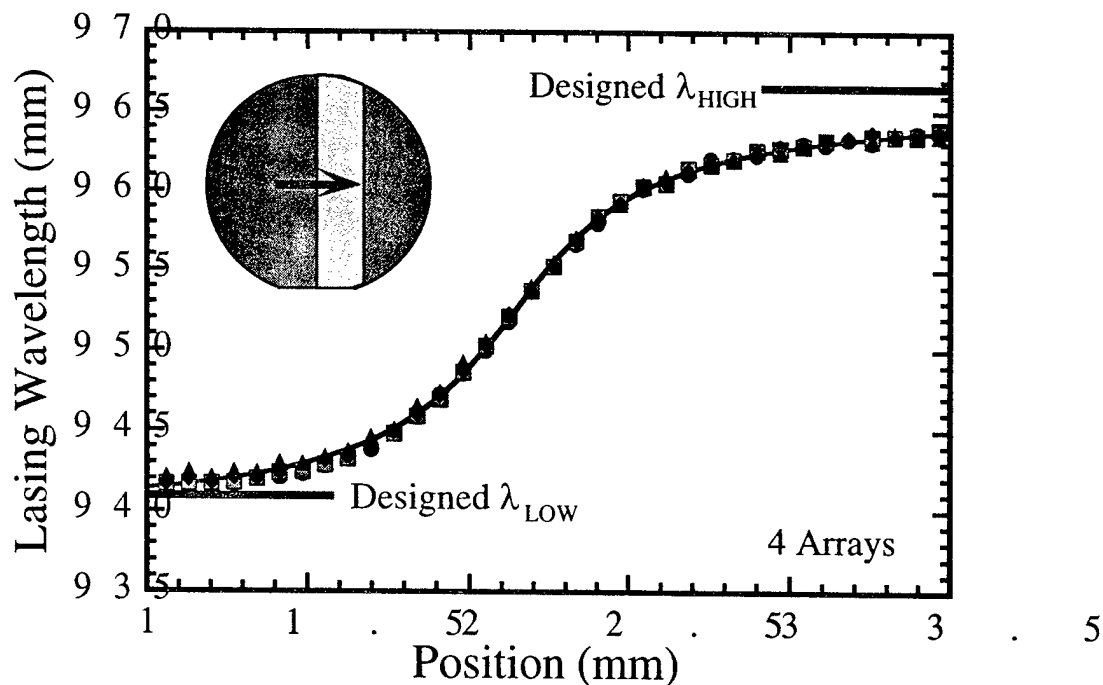


Figure 24. Pulsed lasing wavelengths of four 35-element arrays. The designed high and low wavelengths are marked correspondingly.

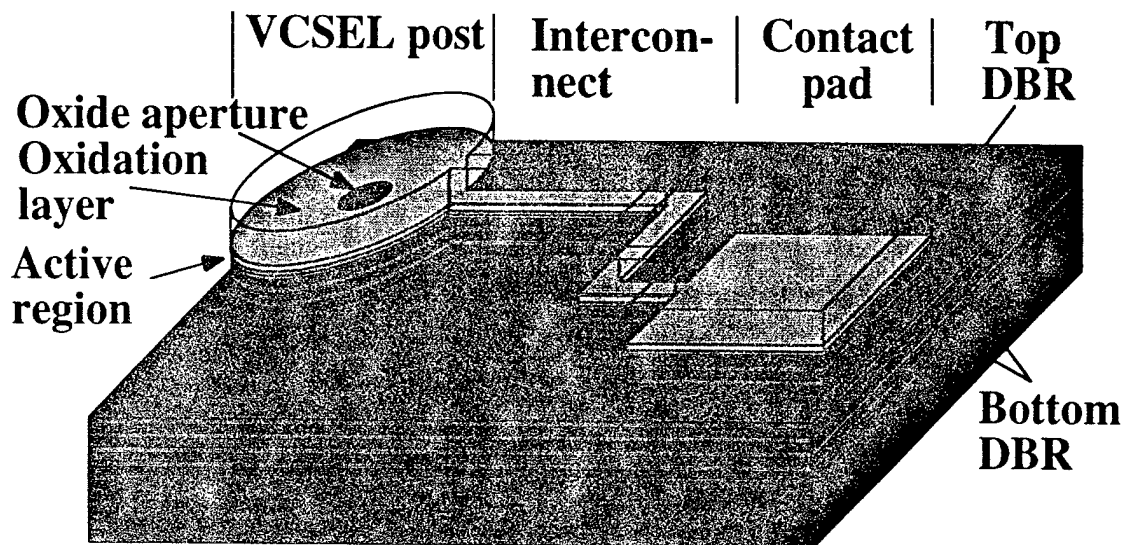
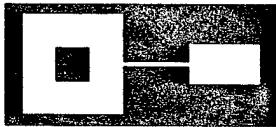


Figure 25. Typical VCSEL structure with the top DBR mirror removed to show the oxidation layer.

Two-mask process

- Interconnect lithography

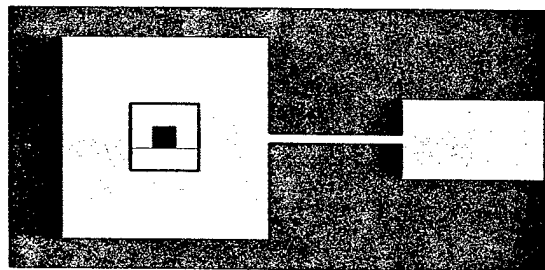


- Au evaporation
- Au lift-off
- Isolation lithography



- Etch
- Oxidation at 425C in water vapor

Top View



Vertical Section

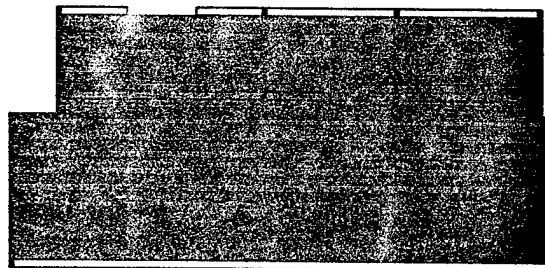


Figure 26. Very simple 2-mask addressable oxide isolated VCSEL array process.

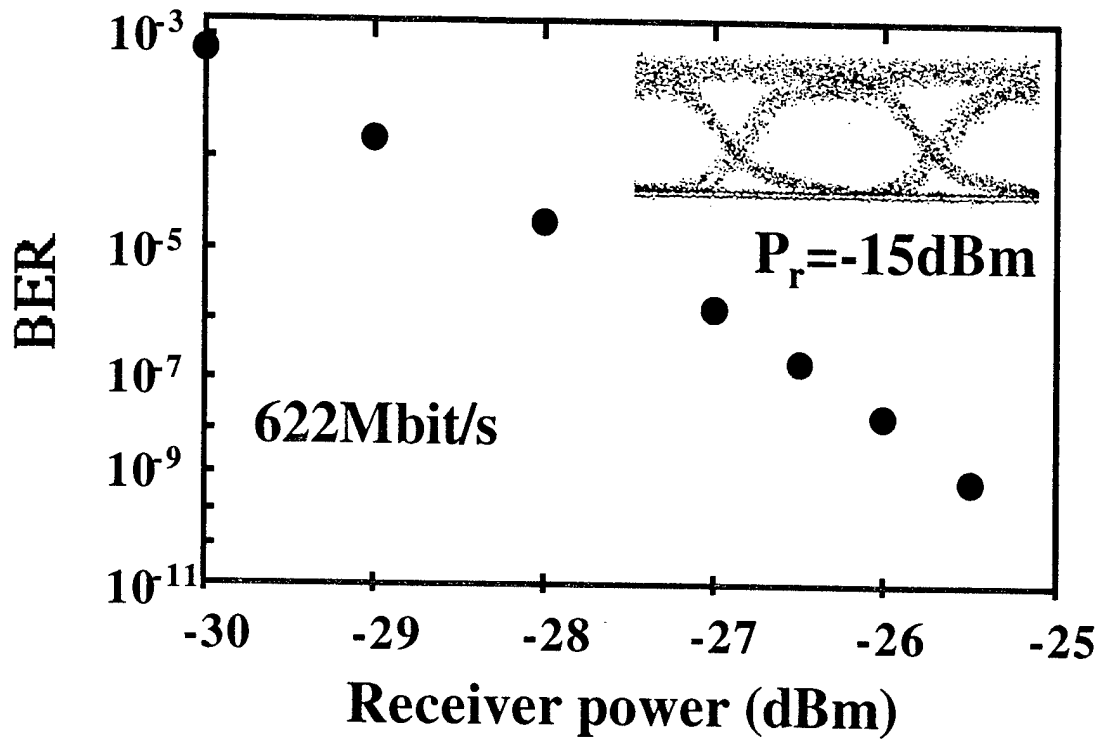


Figure 27. Bit error rate measurements of a typical oxide isolated VCSEL array that show high speed performance of the novel oxide isolated VCSEL process.

Focus Area: Optical Interconnect Information Networks
Task: Optical Interconnects for Multiprocessor Machines
(415-723-1882, goodman@ee.stanford.edu)

Personnel

J.W. Goodman

J. Lam

Summary

Our project was initiated in support of the WDM interconnect project at Stanford, and was aimed at developing a compact, integrated-optic wavelength Mux/Demux suitable for use in the 900 nm region. The design is based on the Dragone architecture, although the particular form of the implementation is different than has appeared in the literature previously.

This design would not have been possible had we not simultaneously developed modifications of beam-propagation code that was able to predict the performance of various designs. The modification we carried out allows beam-propagation to be formulated in cylindrical coordinates, which are appropriate for the particular design we have adopted. Extensive simulations of various device designs were carried out during the course of this project, leading to a set of designs that were actually fabricated on the final wafer.

The design and photomask layout for a series of waveguide grating devices were completed and a finished mask was submitted to PIRI for the fabrication process. These waveguide gratings are the first designed for the 900 nm region, to the best of our knowledge. The mask was designed for a four-inch wafer. The designs included variations in waveguide dimension, grating order and wavelength separation. The waveguide dimension variation helped us understand the effect of mode profile on device performance and efficiency. Multimoding of the waveguides leads to crosstalk between wavelength channels, and an excessively single-mode design leads to excessive loss, especially in bending regions. The fabrication of a number of devices with different dimensions also offers options in the event of refractive index and dimension changes in the fabrication process. Grating order and wavelength separation variations provide information about performance and bandwidth tradeoff of our design geometry. There are a total of 24 devices on the wafer with fourteen different designs. Testing structures were placed in the center of the wafer for light propagation characterization with different bending curvatures. All structures have a 90-degree geometry, in accordance with the geometry of a circular wafer. Dicing marks on the edge and center of the wafer indicate the way wafer will be diced into four quarters, with input/output waveguides on perpendicular edges. The layout was done with 0.1mm grid size using Design Workshop 2000. A picture of the wafer layout is shown in Figure 28.

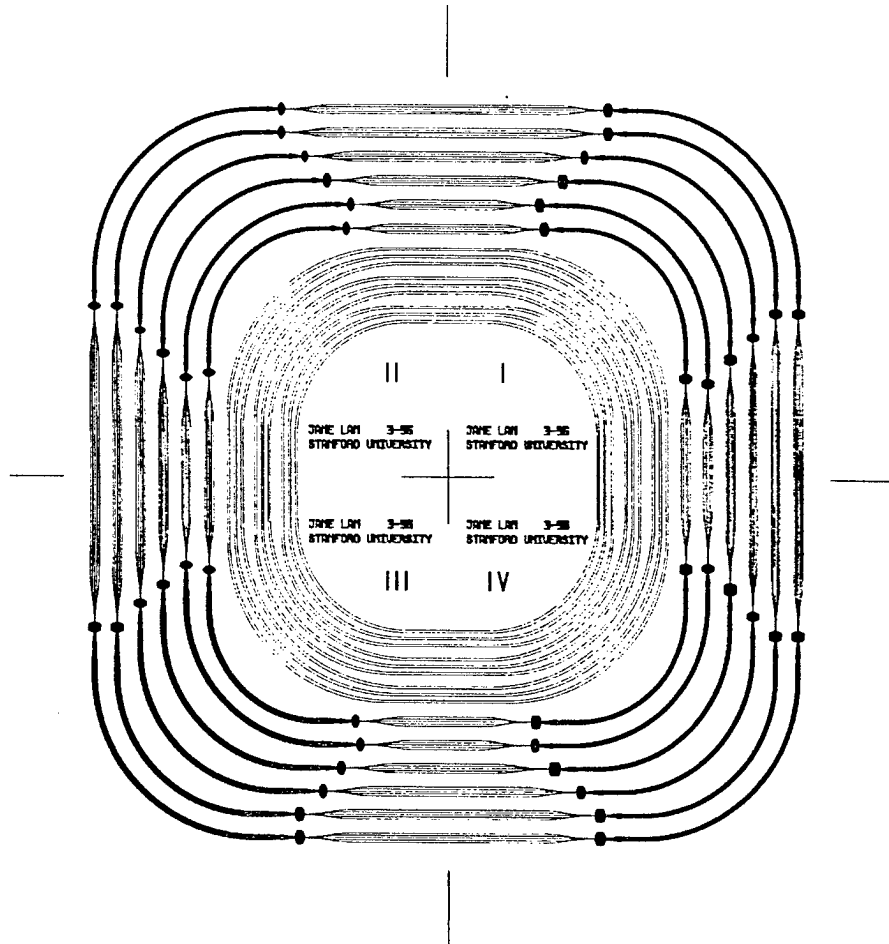


Figure 28. Mask showing wafer layout

A fabricated and diced wafer was received from PIRI and effort during the final quarter of the contract was devoted to measuring the properties of the various designs as wavelength Demux devices. An enormous amount of experimental data was gathered using a scanning laser as the input to the device, and measuring in detail the outputs of the various ports on the devices of different designs. This information will be presented in detail in the Ph.D. thesis of Jane Lam, but space limitations suggest that only an example can be presented here. Figure 29 shows the outputs from various ports of a 7-port device, for which only 5 ports are actually used for output. The input is applied in all cases shown here to the central input port (of five such ports), and the output power on each of five ports was measured as a function of the wavelength of a scanning laser. The five peaks near the middle of this plot represent the responses of each of the five output ports as the wavelength was scanned. The responses at the far left and the far right arise as the wavelength is scanned into a different grating order.

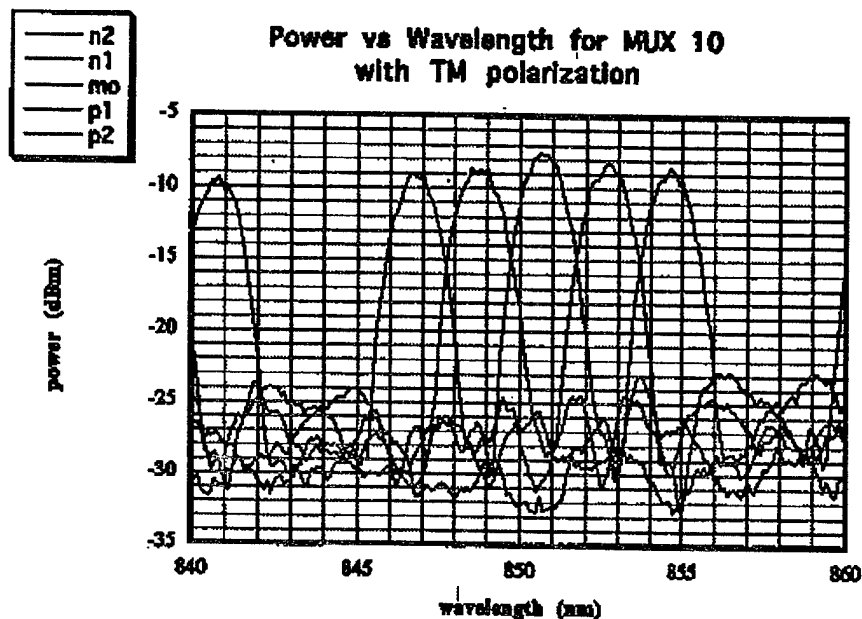


Figure 29. Wavelength scans for waveguide grating device

Typical results were a center wavelength of $850 \text{ nm} \pm 0.3 \text{ nm}$, resolution 2 nm for some devices, 3 nm for others (depending on the design), crosstalk levels down 15 dB for the best devices, and an insertion loss of 1.5 dB relative to a single curved waveguide.

Extensive comparisons between the simulations and the experimental results have been carried out and will be presented in the Ph.D. thesis mentioned above.

Ms. Lam has accepted permanent employment with Roitech in Sunnyvale, CA, and will use the device design experience gained in her thesis to help that company develop commercial products.